2017

Developing Pulse Shape Discrimination Techniques to Identify Alpha Particles, Neutrons, and Gamma Rays

Emily Hudson , '17

DEVELOPING PULSE SHAPE DISCRIMINATION TECHNIQUES TO IDENTIFY ALPHA PARTICLES, NEUTRONS, AND GAMMA RAYS

By

Emily Hudson

A THESIS

Submitted to
Swarthmore College

ABSTRACT

DEVELOPING PULSE SHAPE DISCRIMINATION TECHNIQUES TO IDENTIFY ALPHA PARTICLES, NEUTRONS, AND GAMMA RAYS

By

Emily Hudson

The purpose of this project was to develop pulse shape discrimination (PSD) methods that would be applied to background measurements for the Mitchell Institute Neutrino Experiment at Reactor, or MIνER, collaboration. The purpose of the MIνER experiment is to detect coherent elastic neutrino-nucleus scattering (CEνNS). Pulse shape discrimination is an analysis method used to distinguish between different particles by the shapes of their waveforms. I wrote my analysis code in Python while my research partner wrote her code in C++. We tried a variety of PSD methods. In one method, we curve fit the waveform to various functions and distributions (Gaussian, a piecewise function of two Gaussians, and Landau, among others) while looking at various parameters of the fits. Another method we applied was charge pulse integration, in which we integrated the area of the waveform's curve. My code was tested on simulated data from a CAEN DT5800 desktop digital detector emulator. The charge pulse integration code worked the best for distinguishing between two types of simulated waveforms. If taken further, my Python code would be further developed and tested on real data.

ACKNOWLEDGMENTS

I would like to thank my research partner, Kaitlin Salyer. I thank Dr. Grigory Rogachev, my faculty mentor for this research. I would also like to thank Josh Hooker for his direction and advice. I thank the Cyclotron Institute at Texas A&M for hosting the Research Experience for Undergraduates (REU) program that made the research that this thesis is based on possible. I would like to thank my advisor, Dr. Carol Guess, for her advice and revisions. I would also like to thank Dr. Adam Light, who looked at my thesis for its final revision.

TABLE OF CONTENTS

LIST OF FIGURES

Chapter 1

Introduction

The purpose of this project was to develop analysis tools for pulse shape discrimination (PSD). Pulse shape discrimination is an analysis method used to distinguish between particles based on the shape of their waveforms. The pulse shape discrimination analysis tools developed in the project would then be used in background measurements for MIνER, a larger collaborative experiment searching for coherent elastic neutrino-nucleus scattering (CEνNS). The scattering the researchers wish to detect will produce a recoil signal small enough that background noise will be a problem. This background noise needs to be measured and accounted for so that the researchers can observe and identify events. Pulse shape discrimination is one method to distinguish between different types of background.

Chapter 2

Neutrino physics

2.1 Neutrinos and antineutrinos

2.1.1 Proposal and discovery of the (anti)neutrino

The idea of the neutrino (or antineutrino) was first proposed by Pauli in his 1930 letter and then expanded upon by Fermi in his paper "Theory of β rays" [1]. There are three types of beta decays. It was observed that in beta minus decay, a neutron decays to a proton and an electron. In beta plus decay, a proton decays to a neutron and a positron (the electron's antiparticle, which is positively instead of negatively charged). In electron capture, a proton and an electron combine to form a neutron. These decay equations are shown below.

$$n \rightarrow p + e^- \tag{2.1}$$

$$p \rightarrow n + e^+ \tag{2.2}$$

$$p + e^- \rightarrow n \tag{2.3}$$

According to conservation laws, each side of the equation must be balanced [2]. Since protons are positively charged, electrons are negatively charged, and neutrons have no electric charge, we see that electric charge is conserved. But in addition to electric charge being conserved, angular momentum must also be conserved. The neutron, the proton, and the electron are all fermions and all have intrinsic spins of $S = \frac{1}{2}\hbar$. Thus, one side of the equation will have a half-integral angular momentum and the other side will have an integral relative angular momentum. The two sides will not balance. The presence of another fermion in this equation would balance the relative angular momenta on each side. Another problem with this form for the beta decay equation is that the beta rays were observed to have a range of energies. If there were only two products, then according to conservation of momentum they should exactly share the energy from the decay. The charged particles' tracks also moved in unexpected directions and appeared to violate conservation of linear momentum.

2.1.1.0.1 These problems led Fermi to suggest that a third particle existed. This third particle also had to adhere to conservation laws, so it would have to have specific properties. The new particle would have to be of neutral charge and would have to be an antiparticle to balance the creation of a particle in this decay. This new particle would have to be a fermion, having a half-integral spin so that angular momentum could be conserved. It would also have to have a mass smaller than the instrumental uncertainties. This maximum mass was originally 1 keV but is now 10 eV [3] The cross section for a neutrino (or antineutrino) undergoing a reaction was expected to be small, and so the neutrino or antineutrino would be difficult to detect. A high flux neutrino source would be needed if the researchers expected to see an interaction. Cowan and Reines were the first to detect the antineutrino, using a nuclear reactor as the high flux neutrino source. The reactor would produce ten trillion neutrinos per square centimeter per second [4]. Cowan and Reines hoped to observe a process called inverse beta decay: an antineutrino would collide with a proton and produce a positron (the electron's positively charged antiparticle) and a neutron [5]. After the construction of a prototype, Cowan and Reines built a detector and conducted the experiment at Savannah River. There the detector could be placed close to the nuclear reactor but also 12 meters underground, thus being shielded from cosmic rays that the detector might also pick up. The inverse beta decay reaction should produce two separate bursts of gamma rays [6]. The first would come from the positron right after the reaction as it collides with an electron and annihilates, creating two gamma rays. Detecting the second burst required the use of tanks of cadmium chloride. The cadmium nucleus would capture a neutron about five microseconds after the inverse beta decay reaction, as the neutron would collide with other nuclei and slow down until the neutron was slow enough to be captured. The two described gamma ray bursts were detected in 1956.

2.1.2 Discovery of other neutrino types

So far, the only type of neutrino discussed has been the electron antineutrino. The existence of other types of neutrinos was not realized until the discovery of the pion and observation of its decay. This pion has a mass in between that of a proton and an electron and can be positively or negatively charged, or neutral. Anderson and Neddermeyer observed the pion's decay into a particle called a muon (heavier than an electron, but negatively charged) and a neutrino. An experiment was then done at Brookhaven National Lab by Danby *et al.* to see whether this neutrino was different from the neutrino produced in beta decay [7]. This experiment used protons to produce a beam of pions. These pions would decay, producing muons and neutrinos.

The neutrinos were then isolated by the use of shielding, which did not let charged particles pass through. The neutrinos would then interact with aluminum plates and pass through spark chambers. The researchers expected that if the neutrinos produced in pion decay and in electron decay were different, then they would produce either muons or electrons in the inverse reactions. If the neutrinos from both were the same, then they expected to see a mix of muons and electrons. This experiment found that only muons were produced, so it was concluded that there were distinct types of neutrinos: muon neutrinos and electron neutrinos. Another particle, called the tau particle, was found in 1976 [6]. This particle was negatively charged, like the electron, but was also heavier. At this time, the standard model predicted that every lepton had a corresponding neutrino. This tau particle was categorized as a lepton like the electron and the muon, so it followed that there must be a new corresponding neutrino type. This tau neutrino was not directly detected until 2000, in the Direct-Observation of 'Nu-Tau' (DONUT) experiment.

2.1.3 The weak nuclear force and virtual particles

The weak force is the force by which beta decay occurs, and is also the main force by which neutrinos interact. In 1938, Hideki Yakawa proposed that this weak nuclear force is propagated by a particle: the W boson [6]. It should be noted that in quantum mechanics, electromagnetic interactions are described by the exchange of virtual photons. These virtual photons can carry momentum, and their existence is allowed because of the Heisenberg uncertainty principle, formulated as

$$\Delta x \Delta p_x \leq \frac{\hbar}{2} \tag{2.4}$$

or

$$\Delta E \Delta t \leq \frac{\hbar}{2} \tag{2.5}$$

Under the limit given by the uncertainty principle, a particle can break laws of conservation. A virtual particle can have momentum and jump from one place to another, but it only exists for a very short period of time (the limit of which is given by the uncertainty principle). As the electromagnetic force is propagated through particles called virtual photons, so Yukawa suggested that the weak force propagates through a virtual particle called the W particle (now called the W boson). The W particle, being a virtual particle, would also only be able to propagate over very short distances. This is specifically about 10^{-3} fm, smaller than the size of a nucleon, which is a few femtometers [3]. This W boson is the propagator of the weak nuclear

force in charged current interactions. It also only interacts with particles with left-handed spin. Another virtual particle, called the Z boson, is neutral and propagates the weak nuclear force in neutral current interactions. The Z boson interacts with left-handed or right-handed spin particles. It can also produce identical leptons of opposite charge [6].

2.1.4 Detecting the W and Z bosons

Any experiment seeking to observe these bosons would have to produce many of them. Two CERN experiments (UA1 and UA2) sought to detect these bosons [8] [9]. Both involved use of the Super Proton Synchrotron (SPS) collider. The SPS collider used two high energy beams, one proton and one antiproton. They both had an energy of 279 GeV and would travel in opposite directions. These beams would then collide at two specific locations in the accelerator, and annihilation would occur, producing a lot of energy. The detectors used in the UA1 and UA2 experiments were multi-wire proportional chambers. These detectors contain a gas-filled chamber which in turn contains wires that track the particles. These detectors could only measure charged particles, and would measure the particles' energy and momentum. If there was sufficient energy, the annihilation of protons with antiprotons would produce the W and Z bosons. After its production, the W boson would decay, producing a high energy electron. The Z boson would also decay, producing an oppositely charged pair of high energy electrons or muons traveling in opposite directions. The experiment found many of both of these events. The researchers were also able to measure the mass of the bosons: the W boson mass was found to be about 80 GeV/c^2 and the Z boson mass was found to be about 91 GeV/c^2 [8] [9].

2.1.5 Neutrino helicity and parity

Particles have intrinsic spin: in other words, a particle will rotate about an axis. The component of this spin that is about the particle's axis of motion is called the particle's helicity [6]. This is separate from the particle's total, overall spin. A massless particle will spin about its direction of motion, and so its helicity will also be its total spin. A particle can either spin about its axis of rotation clockwise (right-handed spin) or counterclockwise (left-handed spin). If a massless particle rotates clockwise about its direction of motion, it is said to have right-handed helicity. If it rotates counterclockwise, it has left-handed helicity. An illustration from Solomey shows these helicities (Fig. 2.1) [6].

A type of parity conservation asserts that the laws of physics should be the same

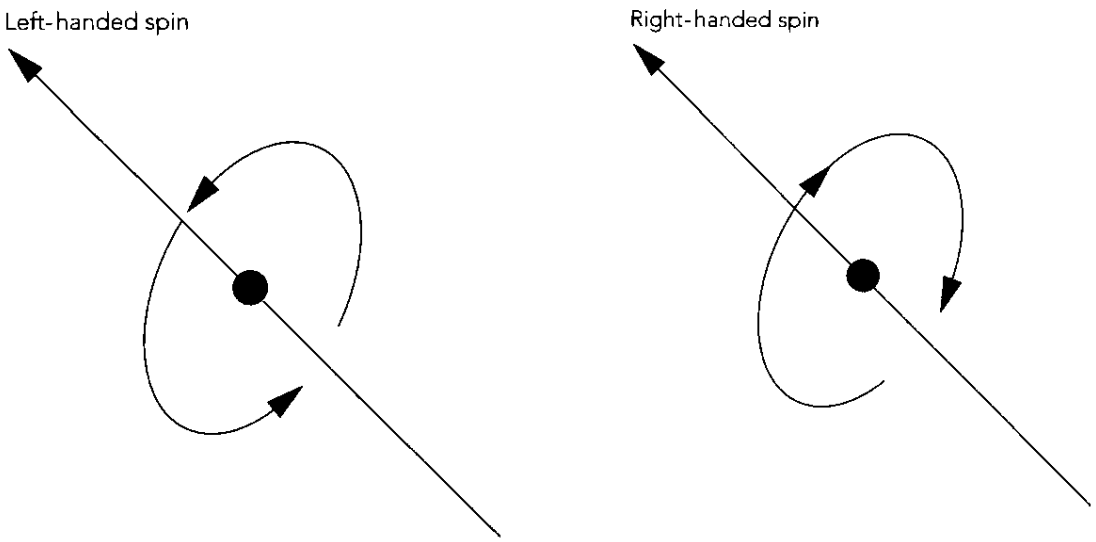

Figure 2.1: This diagram shows right-handed and left-handed helicity. From Solomey, N., *The Elusive Neutrino: A Subatomic Detective Story*, (Scientific American Library, New York, New York, 1997).

for left-handed and right-handed systems. One experiment testing parity conservation was conducted by Chien-Shiung Wu [10]. This experiment would test whether beta decay had a preferential handedness when the spins of the parent nuclei were all aligned in the same direction. In this experiment, the researchers used a cobalt-60 source, which undergoes beta minus decay. The researchers froze the cobalt-60 source and applied an external magnetic field. The temperature at which the cobalt was kept would decrease the atoms' thermal motion and help the atoms' spins to align with the magnetic field. The magnetic field was also applied so that the electrons would travel in one direction or the other, depending on the handedness of the decay. Parity conservation would predict that there would be no preference for handedness, or that an equal amount of electrons would travel in both directions. The results showed a preference for one direction. The researchers performed the same experiment on cobalt at a warmer temperature to test for systematic bias. The preference went away and an equal amount of electrons in either direction was seen, as was expected since now the spins of the cobalt atoms would be very difficult to align. It was shown that in this beta decay, the antineutrinos had a preference for right-handed helicity. As the magnetic field could not align all of the spins of the cobalt atoms perfectly, it was not possible to conclude that the antineutrinos from the beta minus decay were

always right-handed.

2.1.5.0.1 The helicity of the neutrino was later measured in a 1950s experiment by Goldhaber, Grodzins, and Sunyar [11]. To make the calculation easier, the researchers wanted to use a source that decayed via electron capture into an excited state of the product nucleus, that originally had an orbital angular momentum of zero, and the product nucleus of which had an orbital angular momentum of one. Orbital angular momentum is a different type of angular momentum than spin. The only viable source was then europium-152 (^{152}Eu), which decays via electron capture into ^{152}Sm* (the asterisk indicates an excited state), which emits a neutrino. Because of conservation of momentum, the samarium nucleus would also travel away from the neutrino, and both the samarium nucleus and the neutrino would have the same helicity. The researchers could then measure the helicity of the samarium nucleus as it decays from its excited state to its ground state, releasing a gamma ray with energy a little higher than 960 keV. To make this measurement, the researchers also need to be able to measure the gamma rays' polarization and to eliminate background noise from other gamma rays [11]. To account for background gamma rays, the researchers were able to make use of a process called resonant scattering. Pure samarium nuclei can quickly absorb and emit gamma rays (which would have a specific energy) produced by other samarium nuclei. By carefully placing samples of ^{152}Sm, the researchers could direct the gamma rays into a shielded area where background noise would be reduced. To measure the polarization, the researchers placed the ^{152}Eu source inside a magnetic field. By aligning the magnetic field in one direction or the other, the researchers could cause gamma rays of one polarization or the other to be more likely to be absorbed by the electrons of the iron atoms in the magnet. As a result, only gamma rays of one polarization would pass through and be recorded by the detector. The researchers could then reverse the field to record the number of gammas of the other polarization, and comparing the number of gammas of each polarization would give the preference. When this was done, the researchers only recorded left-handed gamma rays, and no right-handed gamma rays except for what was background noise [11]. The results showed that all of the neutrinos were left-handed. It turns out that neutrinos and antineutrinos have opposite helicities.

2.1.6 Antimatter and antineutrinos

Antimatter consists of antiparticles. An antiparticle contains the quantum numbers (electric charge, intrinsic spin, etc.) opposite to those of its corresponding particle [6]. For example, the positron has a positive charge while the electron has a negative

charge. The proton and neutron also have corresponding antiparticles. Though the neutron has a neutral electric charge, it (like the proton) is composed of fundamental particles called quarks, and those quarks also have antimatter equivalents (called antiquarks). Antimatter particles were first predicted by Dirac's equation, which combines quantum electrodynamics with Einstein's theory of special relativity [6]. The behavior of the antiparticles seen so far conforms to this equation. Ettore Majorana suggested that the neutrino might be its own antiparticle. If this were true, then the neutrino would not behave as predicted according to the Dirac equation. If a neutrino could be its own antiparticle, then the antineutrino emitted from beta decay of typical matter would be indistinguishable from the neutrino emitted from beta decay of antimatter. But the neutrino as its own antiparticle would violate lepton conservation, and the neutrino would also have to change its spin from left-handed to right-handed. If the neutrino has no mass, then it would travel slower than the speed of light. Then, depending on the reference frame, the neutrino may appear to change helicity.

2.1.6.0.1 One phenomenon that would, if discovered, give evidence for a Majorana type neutrino would be the discovery of neutrinoless double beta decay. Double beta decay occurs when a nucleus simultaneously undergoes two beta decays. There are two types of beta decay: ordinary double beta decay and neutrinoless double beta decay. The equations for both are below [3].

$$ {}^{A}Z \rightarrow {}^{A}(Z+2) + 2e^{-} + 2\overline{\nu} \tag{2.6} $$

$$ {}^{A}Z \rightarrow {}^{A}(Z+2) + 2e^{-} \tag{2.7} $$

Here, Z represents the nucleus with that atomic number and A gives the mass number of that nucleus. The first has been confirmed and the second has only been suggested. In ordinary double beta decay, a nucleus decays, producing two electrons and two electron antineutrinos. In neutrinoless double beta decay, the antineutrino produced in the first beta decay would transform into a neutrino and be reabsorbed in the second beta decay. This would only be possible if the neutrino is its own antiparticle. Confirmation of the Majorana neutrino or neutrinoless double beta decay has yet to be found.

2.2 Electroweak interactions

2.2.1 Neutrino-electron elastic scattering

Neutrino-electron elastic scattering occurs when a neutrino scatters off an electron, as in the reactions

$$\nu_l + e^- \rightarrow \nu_l + e^- \tag{2.8}$$

$$\overline{\nu_l} + e^- \rightarrow \overline{\nu_l} + e^- \tag{2.9}$$

Here, the l subscript is a stand-in for neutrino type [12]. This type of interaction only involves the weak force. For muon or tau neutrinos, this neutrino-electron elastic scattering occurs through the exchange of a Z-boson. For electron neutrinos, this scattering occurs through both W- and Z-boson exchanges. Consequently, neutrino-electron elastic scattering occurs the most frequently with electron neutrinos [13]. For low neutrino energies, the effects of the propagating bosons can be ignored. The size of the reaction cross sections are affected by the Fermi constant and the weak mixing angle. More information on these factors can be found in *Particle Physics* by Carlsmith and *Fundamentals of Neutrino Physics and Astrophysics* by Giunti and Kim.

2.2.2 Quasielastic charged-current reactions

The quasielastic charged-current reactions are given by

$$\nu_l + n \rightarrow p + l^- \tag{2.10}$$

$$\overline{\nu_l} + p \rightarrow n + l^- \tag{2.11}$$

where l is e, μ, or τ [14]. Only muon and electron neutrino and antineutrino beams are experimentally available; beams of tau neutrinos are only produced in high-energy cosmic ray interactions in Earth's atmosphere and in astrophysical situations. One specific quasielastic charged-current reaction is inverse neutron decay, which takes the form of the latter equation and where the antineutrino is an electron antineutrino.

2.2.3 Elastic neutral-current reactions

Neutrinos and antineutrinos may also elastically scatter off of nucleons in the reactions

$$\nu_l + N \rightarrow \nu_l + N \tag{2.12}$$

$$\overline{\nu_l} + N \rightarrow \overline{\nu_l} + N \tag{2.13}$$

Here N can be a proton or a neutron [14].

The cross-section for elastic neutral-current scattering off a proton is given by

$$\sigma_{NC}^{\nu p} \simeq \frac{G_F^2}{4\pi}[(1-4sin^2\vartheta_W)^2+3g_A^2]E_\nu^2 \tag{2.14}$$

and the cross-section for elastic neutral-current scattering off a neutron is given by

$$\sigma_{NC}^{\nu p} \simeq \frac{G_F^2}{4\pi}[1+3g_A^2]E_\nu^2 \tag{2.15}$$

Here, G_F is a form factor while E_ν is the neutrino energy and ϑ_W is the weak mixing angle [14]. The form factor characterizes the potential energy distribution of the target [15]. The weak mixing angle is a parameter in the theory of electroweak interactions. It is part of a rotation matrix that acts on the Z boson. Further details on the theory can be found in *Particle Physics* by Carlsmith and *Fundamentals of Neutrino Physics and Astrophysics* by Giunti and Kim.

2.2.4 Coherent elastic neutrino-nucleus scattering

Coherent elastic neutrino-nucleus scattering (CEνNS) is a type of elastic neutral-current reaction [16]. It occurs when a neutrino scatters off of a nucleus. Here, the scattering is coherent, meaning that the waves of the off-scattered nucleons are in phase and add coherently. In addition, the nucleus' final and initial states are identical in CEνNS [17]. For coherent elastic neutrino-nucleus scattering to occur, the neutrino must have low enough energy such that the wavelength of the momentum transfer is larger than the nucleus' size. For a spin-zero nucleus, the rate of this reaction is predicted by

$$\frac{d\sigma}{dT}(E,T) = \frac{G_F^2}{2\pi}M\left[2-\frac{2T}{E}+\left(\frac{T}{E}\right)^2-\frac{MT}{E^2}\right]\frac{Q_W^2}{4}F^2(Q^2) \tag{2.16}$$

Here E is the energy of the incident neutrino, T is the nuclear recoil energy, M is the mass of the nucleus, F is the elastic form factor for the ground state, Q_w is the weak nuclear charge, and G_F is the Fermi constant. CEνNS has a large cross-section compared to other processes in the same energy range. This process results in nuclear recoils with energies less than tens of keV [16]. Since these recoils have low energies, very sensitive detectors are needed.

Chapter 3

Radiation Detectors

3.1 Detector Modes

Radiation detectors can operate in one of three modes: pulse mode, current mode, and mean square voltage mode [18]. When we acquired real data with which to test our code, we used the pulse mode of operation. The pulse mode of operation records each quantum of radiation that interacts in the detector, and the output signal is a series of individual signal pulses. Typically, pulse mode operation records the time integral of each current burst (the total charge Q), since this is directly related to the energy deposited in the detector by the radiation. If the detector has a constant capacitance, then the amplitude of each signal pulse is also directly proportional to the corresponding charge generated inside the detector. Measuring the rate at which the pulses occur would also give the rate at which radiation interactions occur inside the detector. When radiation detectors are used to measure the energy of individual quanta this is called radiation spectroscopy. Another use of pulse mode is pulse counting. Here, the detector only records pulses above a certain threshold, regardless of its Q value. This is useful when only information about the radiation's intensity and not its energy distribution is needed. One advantage of pulse mode is that it is typically much more sensitive than current mode or mean square voltage mode.

3.1.0.0.1 In current mode, the detector output is a time-dependent current from a series of events [18]. The detector has a fixed response time T, which is typically longer than the average time between individual event current pulses. Thus, current mode averages out fluctuations between events and records an average current. This average current is a product of the amount of charge per event and the rate at which events occur. This signal from this mode also has a statistical uncertainty from random fluctuations in the event's arrival time. This uncertainty can be reduced by having a large response time T, but this will also slow the detector's response to sudden changes in the rate or nature of events. The mean square voltage mode (some-

times called the Campbelling mode) only makes use of the fluctuating component of the detector current. This fluctuating component is then squared, and the time average of its amplitude is found. This mean squared signal is directly proportional to both the square of the charge produced in each event and to the event rate. The mean square voltage mode is best used when measuring multiple types of radiation: specifically when each type of radiation produces different charges. In this mode, the measurement is weighted towards the radiation with more average charge per event. The information recorded while in pulse mode is important for pulse shape discrimination, so the detectors were operated in pulse mode when we collected data for testing our analysis code.

3.2 Detection efficiency

There are two types of counting efficiencies [18]. Absolute efficiency is the ratio of the number of pulses recorded to the number of radiation quanta emitted by the source. This type of efficiency can be affected by the distance between the radiation source and the detector as well as the properties of the detector itself. Intrinsic efficiency is defined as the number of pulses recorded over the number of radiation quanta incident on the detector. This intrinsic efficiency relies on the energy of the radiation itself, the material the detector is made of, and the thickness of the detector in the incident radiation's direction. The intrinsic efficiency only depends a small amount on the distance between the detector and the source because the path length of the radiation can decrease with distance. For electrically charged radiation such as alpha and beta radiation, the efficiency can be as high as 100 percent. The alpha or beta particle only needs to travel a short distance before it can form enough ion pairs to create a pulse large enough for the detector to record. On the other hand, neutrally charged radiation like neutrons or gamma rays travel for much longer distances before interacting inside the detector. This lowers the detector's efficiency, which would then be useful to know so that one can find the relationship between the number of quanta actually recorded and the number of quanta emitted by the source or the number that hit the detector. The overall efficiency is also affected by whether the researchers set a minimum threshold for a particular event to be recorded. If all of the events that are measured are recorded by the detector, then the efficiency would be appropriately described as the total efficiency. If the only the events that contain the full energy of the incident radiation are included, then this would be the peak efficiency.

3.3 Dead time

Almost all radiation detectors must have some amount of time pass between two separate radiation events in order for the two events to be recorded separately [18]. The minimum amount of time that must pass between the two events is called the dead time. This dead time can result from the detector's own processes or from the electronics used to process the signal. Radioactive decay is random, so it is possible that some incident radiation may not be measured because it interacts during the dead time. This loss is even more likely when the event rate is high. This dead time can be accounted and corrected for through the use of models and by measuring the dead time directly.

3.4 Types of detectors

3.4.1 Scintillation detectors

We used scintillator detectors to test our pulse shape discrimination code. These scintillation detectors will also be used for further measurements of the background radiation at MIνER, when the pulse shape discrimination code will also ideally be used. An ideal radiation detector would satisfy two conflicting criteria. A good radiation detector should be able to support a large electric field but have little or no current flow when there is no radiation. The other criteria is that the radiation should be able to easily knock the electrons off of the atoms in the material, and those electrons should be able to easily travel through it. The first requires an insulator, and the second requires a conductor [2]. The scintillation detector overcomes this issue by combining a scintillator with a photomultiplier tube (PMT). The ionization process occurs in the scintillator. The radiation hits the scintillator and interacts with the atoms in the scintillator, raising them to their excited states. These atoms then de-excite and emit light, or fluoresce. This light then hits a photosensitive surface so that at most one photon produces one photoelectron. These photoelectrons are then amplified inside the photomultiplier tube [2]. Fig. 3.1, from Krane, shows a diagram of a scintillator detector (a scintillator coupled to a PMT) [2].

An ideal scintillation detector would have a number of specific properties. First, the scintillator should efficiently convert the radiation's kinetic energy into detectable light such that the light produced is proportional to the energy deposited by the radiation over as wide a range as is possible. The scintillator should also be transparent to its own emitted light so that it will not be lost. The scintillator's induced fluorescence should also decay quickly enough so that the detector can generate fast

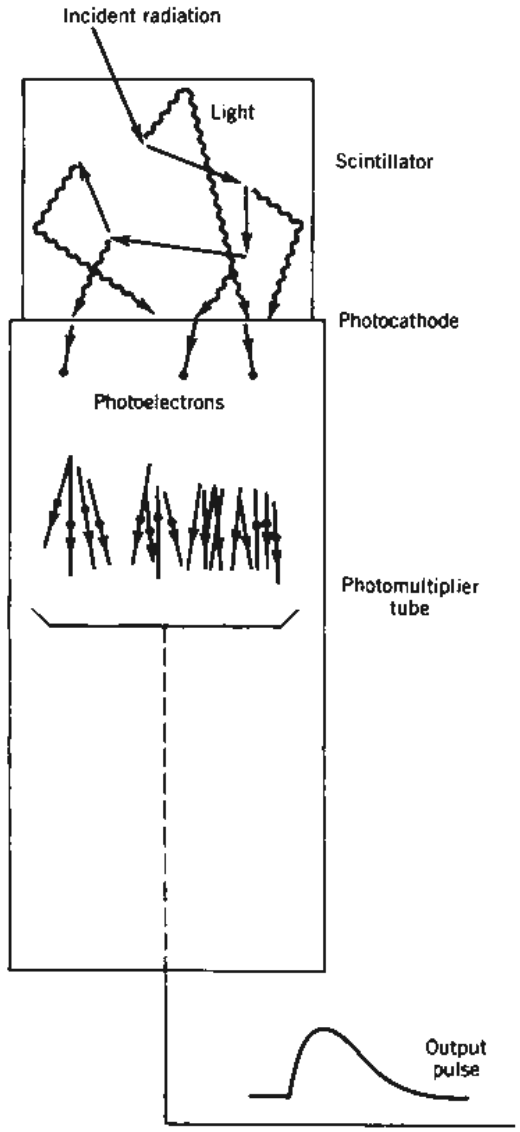

Figure 3.1: A diagram showing how a scintillator detector works, taken from Krane, K. S., *Introductory Nuclear Physics*, (John Wiley & Sons, Hoboken, NJ, 1988).

signal pulses. Here, fluorescence refers to the production of visible light resulting from the de-excitation of the material's excited atoms. The material should also be able to be made in sizes large enough for practical use and should have good optical quality. The material should also have a similar index of refraction to that of glass,

so that the scintillation light can be efficiently passed from the scintillator to the photomultiplier tube or other light detector. No single scintillation material will have all of these properties, so the choice of scintillator will depend on which properties are most important for a particular measurement. A good material will also exhibit prompt fluorescence as opposed to phosphorescence or delayed fluorescence. Phosphorescence occurs when the material emits light of a longer wavelength and with a typically slower characteristic time. Delayed fluorescence is like prompt fluorescence except the atoms have a much longer emission time after excitation occurs [18].

3.4.1.0.1 All of the scintillation detectors used in the experiment are organic scintillation detectors. The atoms in organic scintillators generally become excited from the kinetic energy of charged particles passing through the material. Organic scintillators emit light as a result of transitions in their energy level structure, and so fluorescence can occur regardless of the material's physical state [18]. Many organic scintillators contain symmetries that result in a π-electron structure. These electrons typically do not contribute to the molecule's bonding. Prompt fluorescence typically results from transitions from higher singlet electron energy states to lower singlet electron energy states. The spacing between these electron energy states is usually 3 or 4 eV at most. The electron energy states can also be subdivided into the molecule's vibrational states, where the atoms of the molecule vibrate against each other. These vibrational energies are typically about 0.15 eV apart. At room temperature, all of the scintillator's molecules are in the lowest vibrational state of the electronic ground state. Prompt fluorescence occurs when the molecule transitions from an excited state to one of the vibrational states of the electron ground state. A diagram of an organic scintillator's excited states, taken from Krane, is in Fig. 3.2 [2]. Phosphorescence can also occur in some organic scintillators if an excited singlet state is converted into a triplet state in a process called intersystem crossing. This triplet state takes longer to de-excite and emits a longer wavelength of light. Delayed fluorescence may also occur when the triplet state is excited back to a singlet state, and then decays normally. This delayed fluorescence can show up in the signal as a long-lived tail, called the slow component. This tail can appear different depending on the type of radiation that caused it, and so is useful for pulse shape discrimination [18]. An illustration of these varying shapes is in Fig. 3.3, from Bollinger and Thomas [19].

3.4.1.0.2 Scintillation efficiency refers to how much of the incident radiation's energy gets converted into light. There is a limit on how high this efficiency can be, because it is possible for the excited molecules to de-excite in a way that does not produce fluorescence and instead just produces heat. This is called quenching.

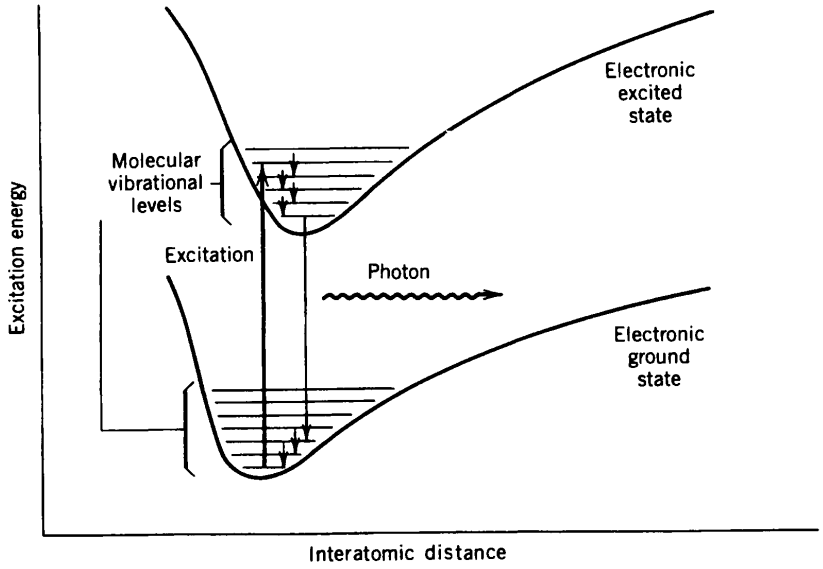

Figure 3.2: A diagram showing the electronic states of an atom of an organic scintillator, taken from Krane, K. S., *Introductory Nuclear Physics*, (John Wiley & Sons, Hoboken, NJ, 1988).

The amount of quenching that occurs will increase if there are impurities in the scintillator, as those impurities will provide more de-excitation modes that do not lead to fluorescence. The excitation energy of an organic material can also be transferred from one molecule to another before de-excitation actually occurs; this occurs in most organic scintillators. The absorption spectra and emission spectra of organic scintillators don't usually overlap, so the light emitted by the material is typically not re-absorbed. Sometimes an organic scintillator may also contain something called a waveshifter. This material absorbs the fluorescent light emitted by the scintillator and emits it at a longer wavelength. This can help lower the amount of reabsorption of the fluorescent light that might occur, and can also adjust the light's wavelength to better match a photomultiplier tube's sensitivity [18].

3.4.1.0.3 Incoming light from the scintillator hits the front of the photomultiplier tube, at which is located a photocathode. This light releases electrons, though a fewer number of electrons than incident photons. These initial electrons then collide with dynodes (a type of electrode) inside the PMT, which have a high probability of releasing a second electron when hit. The dynodes are connected to a voltage chain, and the voltage difference between dynodes is about 100 eV. Electrons then collide

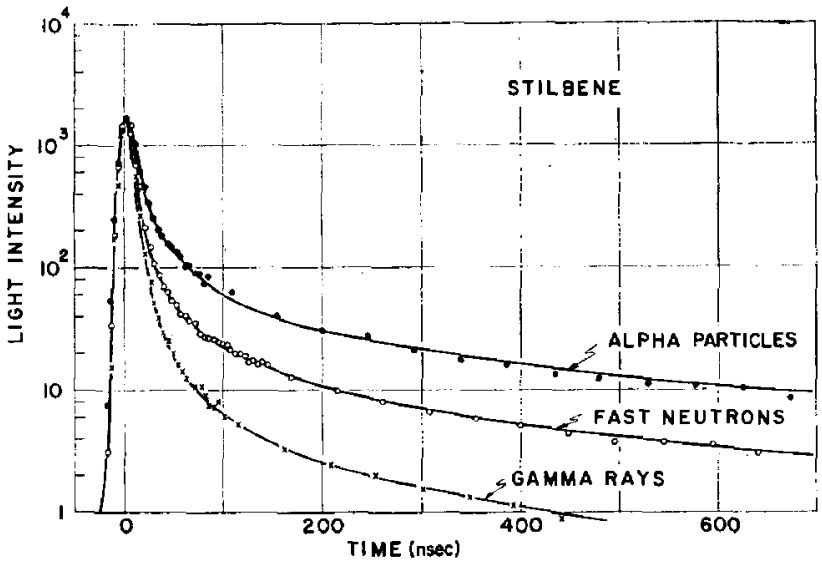

Figure 3.3: This shows the scintillation intensity of a stilbene detector over time, from Bollinger, L. M., and Thomas, G. E., The Review of Scientific Instruments, **32**(9), 1044-1050 (1961).

with the dynode at an energy of about 100 eV. It would take about 2 or 3 eV to emit an electron, so one incoming electron should increase the number of electrons by a factor of 30-50. Yet because the emitted electron may be released in any direction, only about five electrons would actually be emitted at the surface [18]. A diagram from Krane showing this is in Fig. 3.4 [2]

It is also important for the PMT's high-voltage supply to be stabilized. The gain on each dynode depends on the voltage difference between them, so any change in the high voltage will also create a change in the output pulse. This would affect the linearity–the energy deposited in the detector in the radiation should produce a proportional number of scintillation events, and these events in turn should lead to a proportional output pulse from the detector [2]. The PMT and the scintillator can be attached in a number of ways. Sometimes the scintillator and PMT are both in a sealed unit, or the scintillator can be placed in front of the PMT. If the scintillator must be placed far from the PMT, a light pipe can be used to connect the two [2].

3.4.1.0.4 One of the scintillators used to collect real data to test our code was a plastic scintillator. Here, organic scintillators are dissolved in a solvent, which is then polymerized to form a solid plastic [18]. Plastic scintillators can be used for a wide

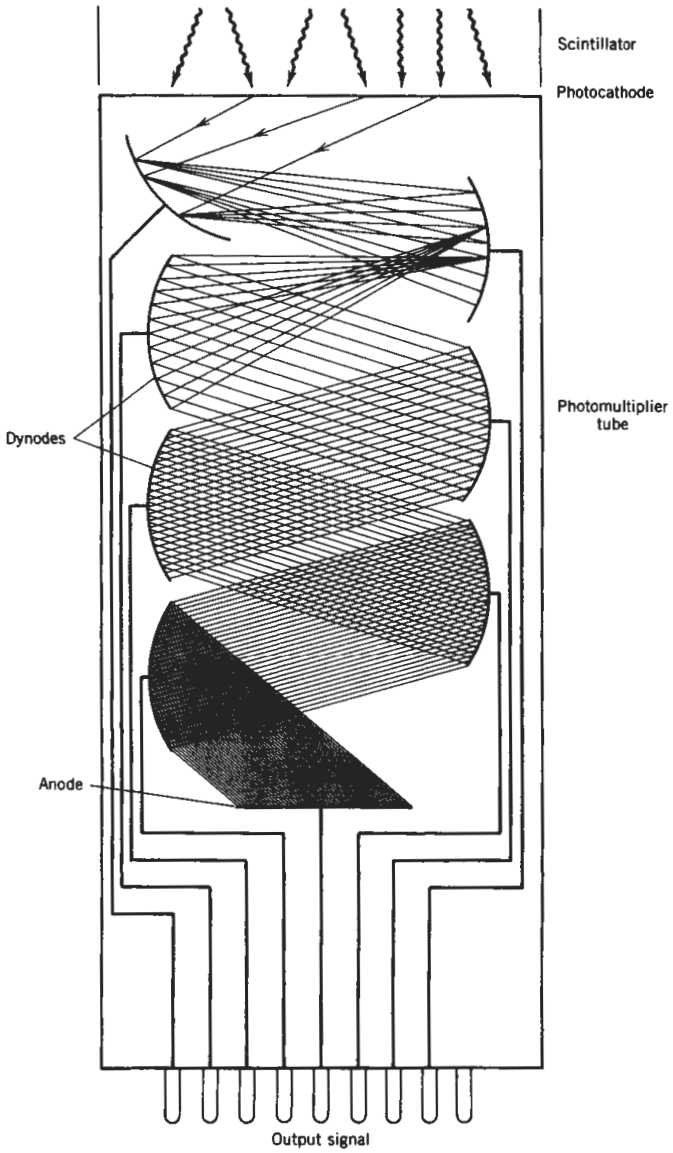

Figure 3.4: A diagram showing how a photomultiplier tube works, taken from Krane, K. S., *Introductory Nuclear Physics*, (John Wiley & Sons, Hoboken, NJ, 1988).

variety of applications because they can be easily shaped and made. They can also be made in large sizes because they are relatively cheap. However, in large scintillators self-absorption may become more of a problem. Another scintillator used to test our code was a stilbene scintillator, which is a pure organic crystal. The scintillation

efficiency of pure organic crystals can be affected up to 20-30 percent by the crystal's orientation [18]. Pure organic scintillators also tend to be fragile, and so getting large pure organic crystal scintillators can be difficult. Stilbene is useful for situations when pulse shape discrimination is necessary, and so it was particularly suited to testing our code [18].

3.4.2 Semiconductor detectors

While the detectors used to collect data to test our code were scintillator detectors, the detectors that will be used at MIνER will be semiconductor detectors. Again, a good radiation detector must produce little to no current when there is no radiation so that background is reduced, be able to support a large electric field, and allow for the easy displacement and travel of electrons [2]. Semiconductors have some important properties and satisfy both criteria well enough. In solids with a lattice structure, electrons have specific energy bands that they are allowed to occupy [18]. In the lower energy valence band, electrons are bound to certain places in the lattice and may participate in bonding. The conduction band is at a higher energy, and the electrons there may flow freely through the lattice. The bandgap separates the valence band and the conduction band. With enough thermal energy, an electron from the valence band can be excited across the bandgap to the conduction band, leaving a hole in the valence band and creating an electron-hole pair. The electron and hole may diffuse to other locations. Fig. 3.5 shows these bands.

If the bandgap is small enough, this excitation is more likely to occur and the material can be called a semiconductor. If an electric field is applied, the electron will tend to move in one direction and the hole in the opposite direction. This is called the drift velocity, and it is proportional to the applied electric field up until a certain point called the saturation velocity. Then an increase in the electric field will not increase the drift velocity further. Most semiconductor detectors have a large enough electric field that this saturation velocity is reached. In intrinsic semiconductors, all electrons in the conduction band must have been excited from the valence band, so every electron in the conduction band must have a corresponding hole in the valence band. The flow of electrons in the conduction band and the flow of holes in the valence band both contribute to the current flowing through the detector.

3.4.2.0.1 Though semiconductors will not typically have these exact properties because of very small impurities, both the germanium detectors and the silicon detectors used in the MIνER experiment are very close. Impurities in the semiconductor can cause electron-hole pairs to be lost [18]. Some impurities (called deep impurities)

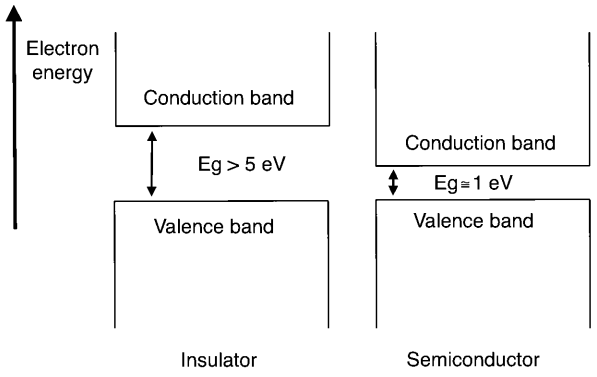

Figure 3.5: This diagram shows the band structure for a semiconductor, from Knoll, G. F., *Radiation Detection and Measurement*, 3rd ed., (John Wiley & Sons, Hoboken, NJ, 2000)..

contain energy levels in the middle of the bandgap, and can trap one of the charge carriers. Other impurities (called recombination centers) can capture both electrons and holes so that they combine and cancel each other out. Charge carrier loss can also occur because of structural defects in the detector. When ionizing radiation enters a semiconductor detector, it produces a number of electron-hole pairs along its path. The average energy the charged particle loses to create one electron-hole pair is called the ionization energy; this ionization energy does not depend on either the radiation's own energy or type. The number of electron-hole pairs produced in the detector then corresponds to the radiation's energy. Since the ionization energy for semiconductor detectors is small, many more charge carriers are created and the energy resolution is better. The energy resolution is also related to the variance in the number of charge carriers. The Poisson model predicts that the variance should be equal to E/ϵ, though the actual variance tends to be smaller. The Fano factor relates the two and is defined as

$$F \equiv \frac{\text{observed statistical variance}}{E/\epsilon} \tag{3.1}$$

Having a small Fano factor would indicate a good energy resolution [18].

The incident radiation creates electron-hole pairs as it passes through the detector, and under the influence of an electric field these pairs travel, creating currents. One of the currents will tend to last longer than the other. To find the induced charge, the two currents are integrated with a long time constant. Semiconductor detectors also have electrodes placed at either end to collect the charge carriers. These electrodes are typically blocking or noninjecting electrodes, so collected charge carriers are not replaced. This decreases the amount of current flowing through the semiconductor [18].

Chapter 4

MIνER

The purpose of MIνER is to detect CEνNS and measure the reaction's cross section. It will take place at the Nuclear Science Center (NSC) at Texas A&M University. It will use semiconductor detectors that use the Neganov-Luke phonon amplification process, which makes detection of CEνNS possible. [20]. The reactor used in MIνER will be a megawatt-class TRIGA (Training, Research, Isotopes, General Atomics) pool reactor with low enriched or 20% uranium-235. This reactor is a source of electron antineutrinos. Detectors can be placed as close as 1 m from the reactor and has a movable core. The distance between the detector and the neutrino source can then be varied [21].

4.1 The Neganov-Luke effect

Some detectors measure the amount of energy the incident radiation deposits in the detector by measuring the amount of ionization in the detector. This is given by the equation

$$N = \frac{E}{\epsilon} \tag{4.1}$$

where N is the average number of pairs of charge carriers produced in the detector, E is the energy deposited in the detector, and ϵ is the average energy used to create one charge carrier pair [22]. The root mean squared fluctuation of the energy is given in

$$\sigma_E = \sqrt{FE\epsilon} \tag{4.2}$$

where F is the Fano factor. This rms value and the electronic noise both contribute to the detector's energy resolution. The noise's contribution to the energy resolution becomes much greater at lower energies. This makes it difficult to detect events below a certain energy threshold. Typically, amplifiers are used to measure the detector's ionization by measuring the current induced by the collection of charge carriers. However, the electronic noise can be further lowered through using a low-temperature

calorimetric method to measure the ionization, which will also lower the energy threshold above which events can be detected. This method works by measuring the heat generated during charge carrier collection, or the number of phonons (quanta of vibrations) produced. If all of the charge carriers are collected and all of their energy is converted into heat, then the thermal energy produced by the incident radiation is given by

$$E_t = \frac{E}{\epsilon} eV_d + E \tag{4.3}$$

Here V_d is the voltage across the detector [22]. This thermal energy can then be found by measuring the detector's change in temperature (typically done with a calorimeter consisting of a semiconductor thermistor), which is approximated by

$$\Delta T = \frac{E_t}{C} \tag{4.4}$$

C is the detector's heat capacity [22]. The root mean square energy noise for such a system would be

$$\sigma_E = \xi \sqrt{k_B T^2 C} \tag{4.5}$$

where ξ is a numerical constant based on the thermistor's responsivity [22]. Pure dielectric crystals at low temperatures also have the relation

$$C \propto MT^3 \tag{4.6}$$

where M is the crystal's mass [22]. The root mean square energy noise can then be very small at low temperatures.

The electronic noise for a detector using this method would then be expressed as

$$\frac{\xi \sqrt{k_B T^2 C}}{1 + eV_d/\epsilon} \tag{4.7}$$

With this method, the electronic noise can be very small at low temperatures, perhaps even so small that one charge carrier pair can be detected [22]. This method can be applied to semiconductor detectors, but not scintillation detectors: while semiconductor detectors make use of charge carrier pairs, scintillation detectors do not. This is why the scintillator detectors will be used for background radiation measurements while the semiconductor detectors will be used in the actual experiment for detecting CEνNS.

4.2 The Nuclear Science Center reactor

The reactor that will be used in the MIνER experiment is a TRIGA (Training, Research, Isotopes, General Atomics) class reactor produced by General Atomics. It is an open pool reactor. Surrounding the reactor pool is approximately 2 meters of dense (about 3.5 g/cm^3) concrete shielding for the neutron and gamma radiation. This wall also contains a cavity (called the thermal column) located on the same horizontal plane as the reactor core. This cavity has multiple benefits: the concrete helps to shield from cosmic ray muons, there is room to place optimal shielding between the core and the detectors, and an area close to the core can be accessed. A diagram of the reactor and experimental cavity, as well as a photograph of the experimental cavity from Agnolet *et al.* is in Fig. 4.1 and Fig. 4.2, respectively [21].

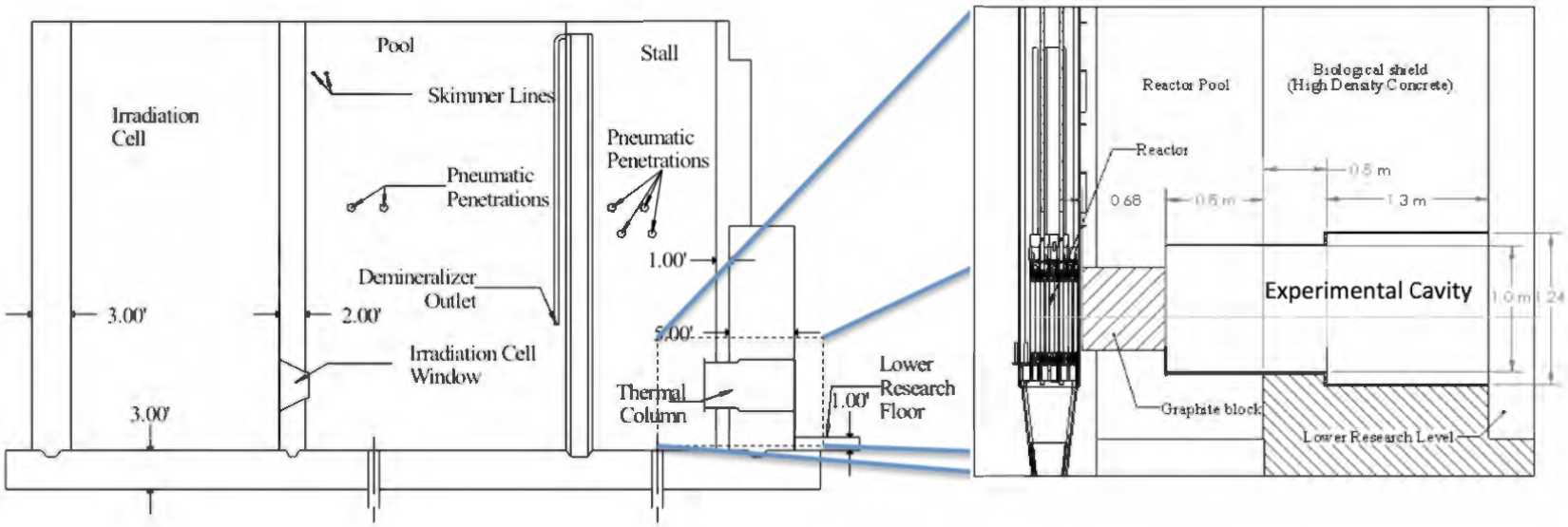

Figure 4.1: A diagram showing the side view of the reactor pool and the experimental cavity, taken from Agnolet, G. *et al.*, Nuclear Instruments and Methods in Physics Research A (2016).

Figure 4.2: A photograph of the experimental cavity, taken from Agnolet, G. *et al.*, Nuclear Instruments and Methods in Physics Research A (2016).

4.3 Accounting for Noise

One of the obstacles that will have to be dealt with in this collaboration is the presence of gamma and neutron background signals from the nuclear reactor. Other backgrounds that must be accounted for include ambient gamma rays and cosmic radiation, the latter of which includes muons and neutrons induced by cosmic rays. Simulations and background readings were done to determine what background radiation would be present during the experiment [21]. This would help the experimenters determine how the background radiation could be reduced and accounted for. This was done in addition to the pulse shape discrimination analysis we hope to apply. One of the simulations was a model of the reactor core done in MCNP (Monte Carlo N-Particle). The simulation gave a neutron energy spectrum which had a fast component (over 100 keV in kinetic energy) flux of $5.8 \times 10^{11} cm^{-2} s^{-1}$ and a slow component (less than 0.625 eV of kinetic energy) flux of $7.7 \times 10^{12} cm^{-2} s^{-1}$. The simulated gamma spectrum showed a total flux of $9.0 \times 10^{11} cm^{-2} s^{-1}$. To reduce the neutron radiation, the experimenters can use a moderator to slow the fast neutrons, which can then be shielded against with a thermal neutron absorber. The gamma radiation can be shielded against with lead or another highly dense material. A simulation was also

done of the experimental hall, this time in the GEANT4 network. The simulation included models of the reactor core, shielding (including its composition), and the detectors or experimental cavity. Neutron, gamma, and muon background measurements of the experimental cavity have also been done [21]. The gamma background measurements were done with a high purity germanium detector. A cylindrical shield of 4" low activity lead was used. Measurements were made with the reactor core off, at 1 kW, at 98 kW, and at 500 kW at three distances: 2.83 m, 3.33 m, and 3.83 m. The gamma background radiation consists of radiation produced by the reactor core and other sources like activated materials. The background that was measured with the reactor off was subtracted from the other background measurements so that the background could be compared to the simulation's results. The spectra shape of the simulation and the background measurements matched each other. A comparison of the simulation's predicted events and the actual measured events for the high purity germanium detector are shown in Fig. 4.3 [21].

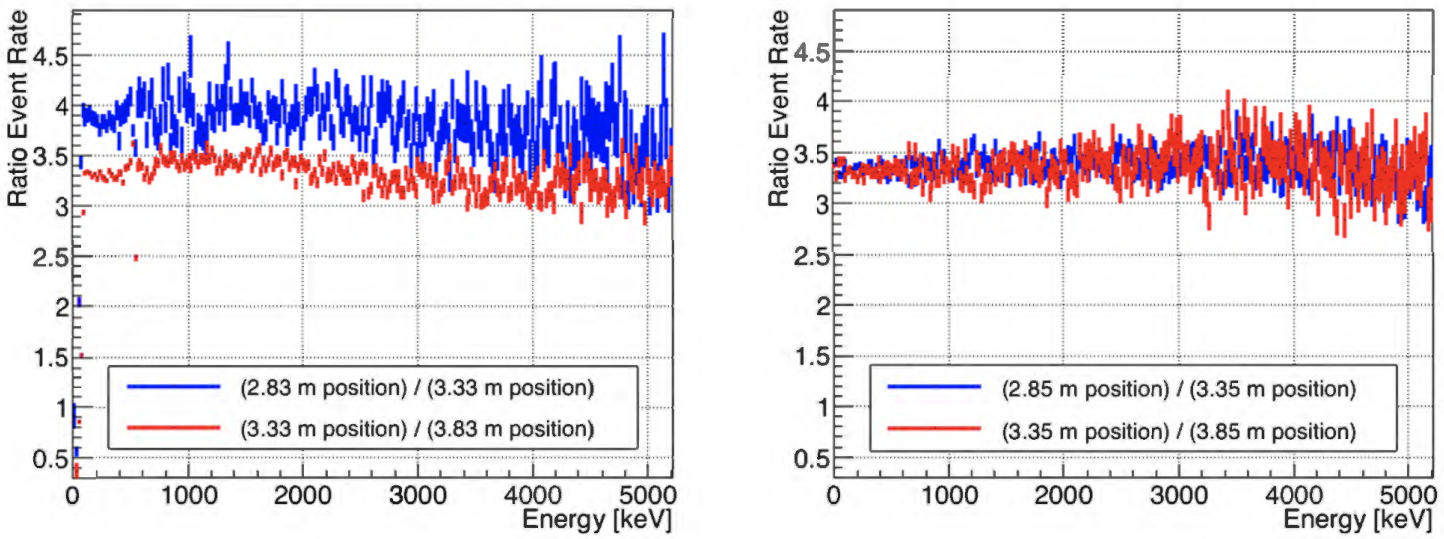

Figure 4.3: The graph for the measured data is on the left and the graph for the simulation is on the right. These graphs show the event rate scaling as a function of the energy deposited in the detector for multiple reactor core positions. From Agnolet, G. *et al.*, Nuclear Instruments and Methods in Physics Research A (2016).

For the neutron background, only the thermal neutron flux was measured. This was done by placing a 6 × 6 inch copper foil inside the experimental cavity. This foil would absorb the thermal neutrons, and so the integrated neutron flux could be found

by measuring the foil's activation. The measured thermal neutron flux matched with the simulation's prediction within 5%. The researchers also tested how effectively the high density concrete wall might shield from cosmic muons. Two polyvinyltoluene scintillator detectors were put inside the cavity and set to trigger for muons. When both scintillators triggered above a threshold within 3 ns within each other, a coincidence signal was produced. Random coincidence events were accounted for by delaying one detector by 150 ns and placing the detectors in the area with the most radioactivity to find the maximum number of random coincidence events they could expect. After finding that they would not need to subtract out random coincidence events, the muon background measurements were made. It was found that the muon background radiation was reduced by about 50% inside the cavity [21].

Chapter 5

Experimental Methods

5.1 Writing the code

For the majority of this project, we wrote code with which we could analyze data using various pulse shape discrimination techniques. I wrote code using the Python programming language while my partner, Kaitlin Salyer, worked on the same project in C++. During most of the writing process, we tested our code with simulated data created using a CAEN V1743 digitizer and a CAEN DT5800 desktop digital detector emulator. The very first step was to write the code that would read the data file, extract the data, and plot the waveform. After that was done, we attempted various curve fits on the waveforms to achieve pulse shape discrimination. The goal was to be able to use the parameters given by the curve fit to distinguish between waveform shapes and therefore their corresponding particles. An example of a simulated waveform is shown in Fig. 5.1.

The first curve fit we tried on the simulated data was a Gaussian fit, which has the form

$$f(x) = Ae^{-\frac{(x-\mu)^2}{2\sigma^2}} \tag{5.1}$$

It is shown in Fig. 5.2.

It did not fit the waveform particularly well, so we then used a piecewise function of two Gaussians where the two pieces were

$$\begin{cases} Ae^{-\frac{(x-\mu)^2}{2\sigma_1^2}} & x \leq \mu \\ Ae^{-\frac{(x-\mu)^2}{2\sigma_2^2}} & \mu \leq x \end{cases}$$

The two pieces of this function would share the same mean "μ", or center, but have different widths. An example of this fit is shown in Fig. 5.3. This fit was better

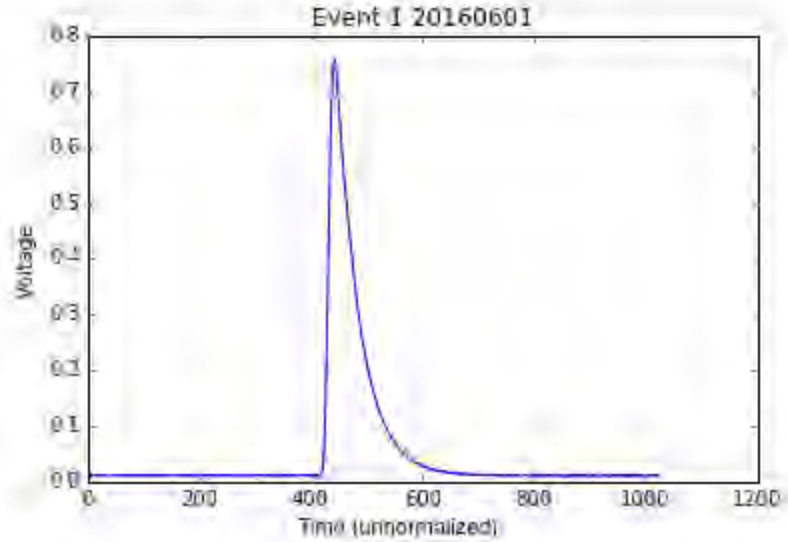

Figure 5.1: This is an example of a simulated waveform. The x-axis is time, though this graph has not been normalized and so one unit corresponds to one data point.

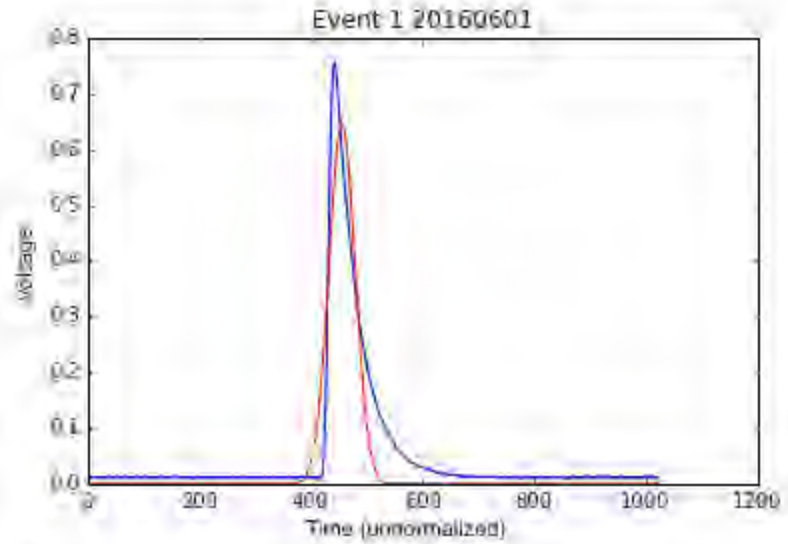

Figure 5.2: A Gaussian fit to a simulated waveform. The x-axis is time, though this graph has not been normalized and so one unit corresponds to one data point.

but not perfect. The fit's maximum did not line up with the waveform's maximum, and it did not match the waveform's tail as well.

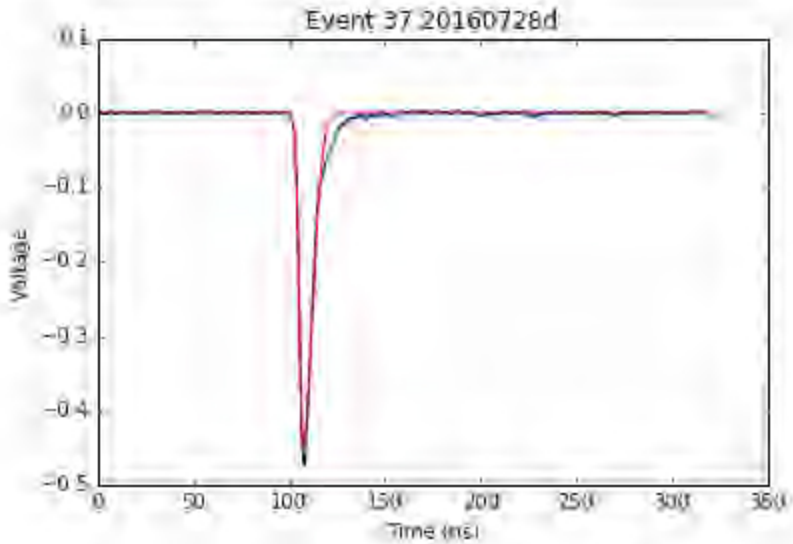

Figure 5.3: A simulated waveform fit with a piecewise function of two Gaussians

We also tried fitting a Landau distribution, which has the probability density function

$$f(x) = \frac{1}{2\pi i} \int_{c-i\infty}^{c+i\infty} e^{s \ln s + xs}\, ds \tag{5.2}$$

This resulted in a fit comparable to the two-Gaussian fit. An example of the Landau fit is shown in Fig. 5.4.

We also tried truncating the waveform and then applying the curve fit. Here, we cut off the data before the waveform's peak, and then only fit to the data after the waveform's maximum, or the falling part of the waveform. Some of these yielded a much better fit for the sample data, particularly the 2-Gaussian fit and the Landau fit (Fig. 5.5 and Fig. 5.6).

The next form of pulse shape discrimination we attempted was the charge integration method (also called the charge comparison method). An article by Gamage *et al.* explains the charge pulse integration method and compares it to other pulse shape discrimination techniques [23]. This method involves integrating to find the area under the waveform. It is a comparison of two integrals of the waveform, each done over a separate interval. One interval is longer and covers the entire pulse while

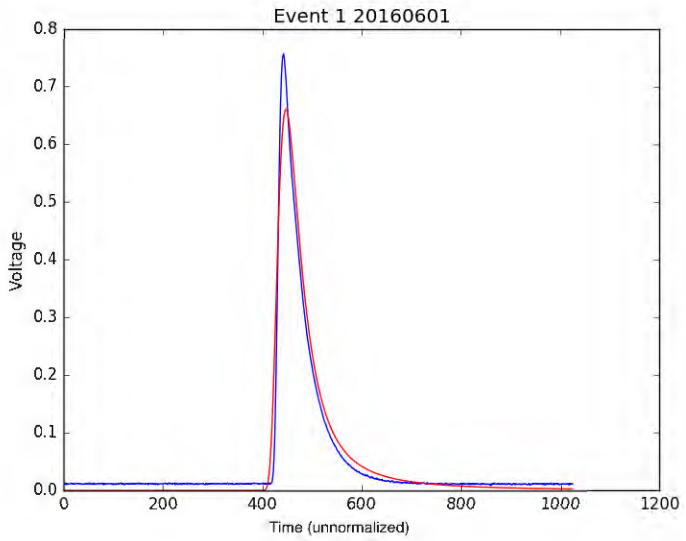

Figure 5.4: A simulated waveform fit to a Laundau distribution. The x-axis is time, though this graph has not been normalized and so one unit corresponds to one data point.

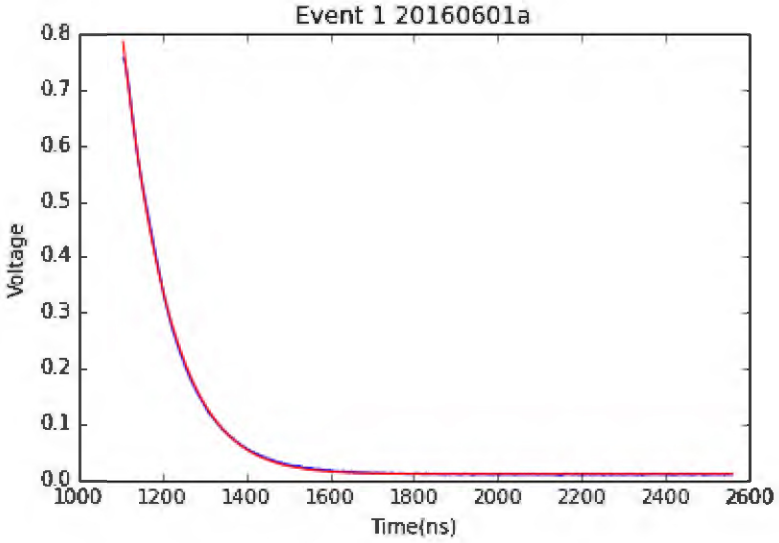

Figure 5.5: An example of the 2-Gaussian fit applied to the truncated data.

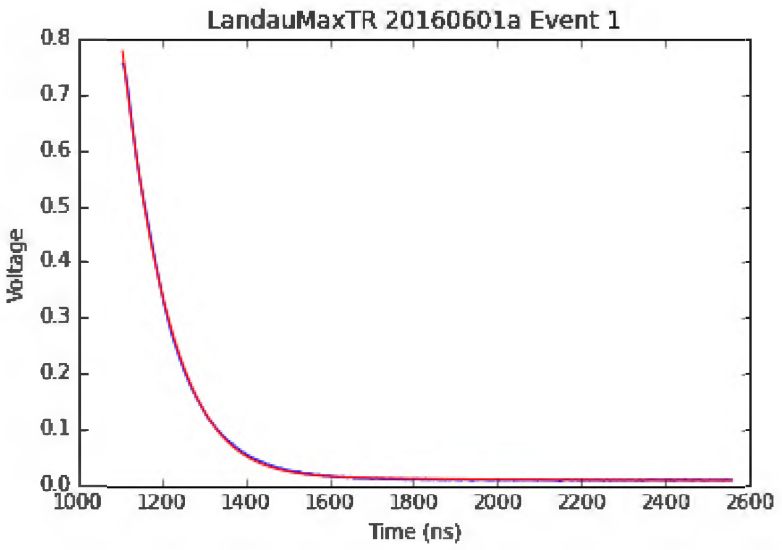

Figure 5.6: An example of the Landau fit applied to the truncated data.

the other interval is shorter and only covers the main peak of the pulse. An image of the interval windows overlayed on the waveform is shown in Fig. 5.7.

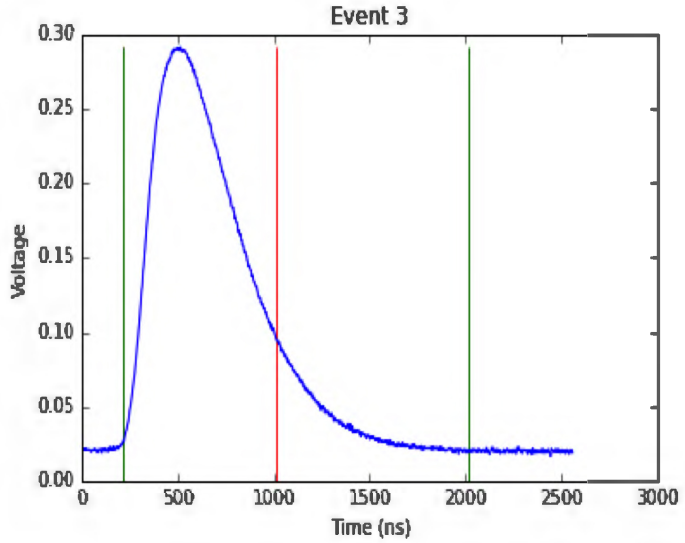

Figure 5.7: A graph showing the intervals for the integral on a simulated waveform.

We obtained a charge value for each integral, which we called Q. We then plugged these values into the formula below, where Q_L stands for the value from integrating the long window and Q_S stands for the value from integrating the short window. This gave us a ratio of the difference between the windows over the long window.

$$PSD = \frac{Q_L - Q_S}{Q_L} \tag{5.3}$$

5.2 Testing the code with real data

Our PSD code was tested using real data, though my partner's code ran much more quickly than mine. My code had a number of efficiency bugs that needed to be eliminated before it could be used feasibly, and the time I was given to do this project prevented from my refining my code further. My partner's code was tested on data collected from two scintillators. Sources of ^{252}Cf and ^{60}Co were used, both measured with a stilbene detector. The code was then tested on data collected from a plastic scintillator, once with a ^{252}Cf source and once with an alpha source. A diagram of the experimental setup is shown in Fig. 5.8. Photos of the plastic scintillator and its PMT are in Fig. 5.9 and Fig. 5.10. A photo of the stilbene scintillator and its PMT is in Fig. 5.11.

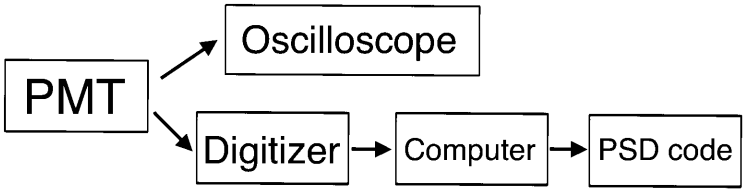

Figure 5.8: A diagram showing the setup for testing our code on real data.

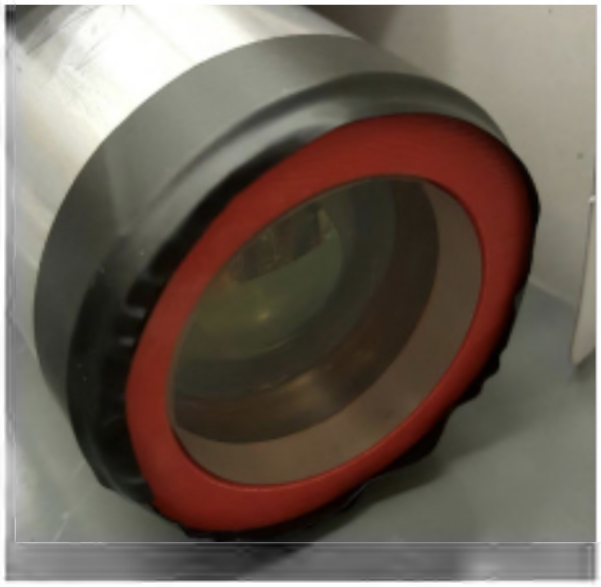

Figure 5.9: A photograph of the plastic scintillator, taken by Kaitlin Salyer. The red piece was 3D printed to hold the plastic scintillator inside the case.

Figure 5.10: A photograph of the plastic scintillator coupled to a PMT, though most of the detector is hidden by the case and the foil.

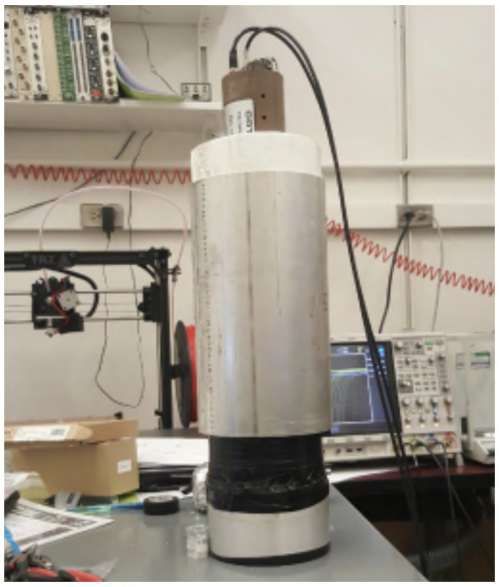

Figure 5.11: A photograph of the stilbene scintillator and its PMT, taken by Kaitlin Salyer.

Chapter 6

Results

6.1 The charge integration method

We chose to focus on the charge integration method, as it was the most useful for distinguishing distinct wave shapes. To test the charge integration method, we created two sets of simulated data. Each set had its own distinctive waveform. We then mixed the two sets together and tested whether or not we could distinguish between them. The waveforms varied in tail size and varied quite a bit in amplitude. We used the charge integration method for these tests. To compare the waveforms, we plotted the amplitudes against the waveform's calculated PSD value. The plot is shown in Fig. 6.1.

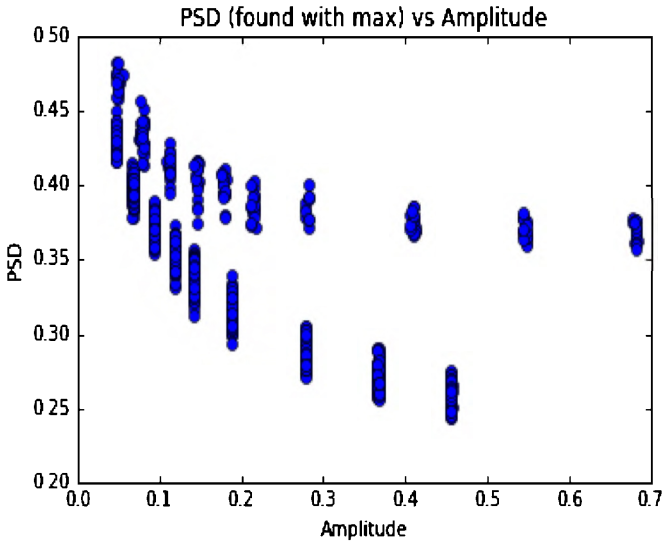

Figure 6.1: A plot showing the simulated waveforms' PSD value vs. their amplitude.

For the simulated data, the charge integration method worked rather well, as Fig. 21 shows two different curves. It is possible to distinguish between two different wave shapes, as some waves have a larger PSD value compared to their amplitude while others do not. This preliminary test is how far I had managed to get in developing and testing my code. The next step would be to refine the code and test it on real data.

Chapter 7

Conclusion

The purpose of this project was to write code for pulse shape discrimination that might be implemented in the larger MIvER collaboration. It is important that the researchers be able to measure and account for background noise in the experiment, and pulse shape discrimination is one way of doing so. We tried a variety of pulse shape discrimination methods, but the one that worked the best was the charge integration method. We were able to successfully distinguish between two different types of wave shapes when we tested this method on simulated data. It's a good start in developing pulse shape discrimination for the MIνER collaboration. The next step in this project would be to continue developing the code and testing it on real data. This would include making the Python code run more quickly and then testing it on real data. We then might try plotting the PSD value obtained from the charge integration method against other waveform parameters. Once the code provides good pulse shape discrimination, it should then be applied in background measurements in MIνER so that the researchers will know how much of each type of background to account for.

BIBLIOGRAPHY

BIBLIOGRAPHY

[1] Wilson, F. L., American Journal of Physics, **36**(12), 1150 (1968).

[2] Krane, K. S., *Introductory Nuclear Physics*, (John Wiley & Sons, Hoboken, NJ, 1988).

[3] Loveland, W., Morrissey, D. J., and Seaborg, G. T., *Modern Nuclear Chemistry*, (Wiley, Hoboken, NJ, 2005).

[4] Close, F, *Neutrino*, (Oxford University Press, Oxford, UK, 2010).

[5] Cowan, C. L., Jr., *et al.*, Science, **124**(3213), 103-104 (1956).

[6] Solomey, N., *The Elusive Neutrino: A Subatomic Detective Story*, (Scientific American Library, New York, New York, 1997).

[7] Danby, G., *et al.*, Physical Review Letters, **9**(36), 36-44 (1962).

[8] Arnison, G., *et al.*, Physics Letters B, **122**(1), 103-116 (1983).

[9] Banner, M., *et al.*, Physics Letters B, **122**(5-6), 476-485 (1983).

[10] Wu, C. S., *et al.*, Phys. Rev., **105**, 1413-1415 (1957).

[11] Goldhaber, M., Grodzins, L., and Sunyar, A. W., Phys. Rev., **109**, 1015-1017 (1957).

[12] Barger, V., Marfatia, D., and Whisnant, K, *The Physics of Neutrinos*, (Princeton University Press, Princeton, NJ, 2012).

[13] Class for Physics of the Royal Swedish Academy of Sciences, Scientific Background on the Nobel Prize in Physics 2015.

[14] Giunti, C., and Kim, C. W., *Fundamentals of Neutrino Physics and Astrophysics*, (Oxford University Press, Oxford, 2007).

[15] Carlsmith, D., *Particle Physics*, (Pearson, Glenview, IL, 2013).

[16] Scholberg, K., Journal of Physics: Conference Series, 606, (2015).

[17] Barbeau, P. S., Nuclear and Particle Physics Proceedings, 265-266, 117 (2015)

[18] Knoll, G. F., *Radiation Detection and Measurement*, 3rd ed., (John Wiley & Sons, Hoboken, NJ, 2000).

[19] Bollinger, L. M., and Thomas, G. E., The Review of Scientific Instruments, **32**(9), 1044-1050 (1961).

[20] Mirabolfathi, N. *et al.*, Nuclear Instruments and Methods in Physics Research A, 1 (2017).

[21] Agnolet, G. *et al.*, Nuclear Instruments and Methods in Physics Research A, (2016).

[22] Luke, P. N., *et al.*, Nuclear Instruments and Methods in Physics Research A, **289**(3), 406(1990).

[23] Gamage, K. A. A., Joyce, M. J., and Hawkes, N. P., Nuclear Instruments and Methods in Physics Research A, **642**, 78 (2011).

[24] Basdevant, J., Rich, J., and Spiro, M., *Fundamentals in Nuclear Physics*, (Springer, Ecole Polytechnique, France, 2005).

APPENDICES

Appendix A

My Python code

Here is the code I used to read the data file, plot the waveform, calculate the long and short integrals, and write the results to a data file.

```
# -*- coding: utf-8 -*-
"""
Spyder Editor

This is a temporary script file.
"""
f=open('20160707a.dat','r')

import matplotlib.pyplot as plt
import numpy as np
#from math import exp
from scipy.optimize import curve_fit
#from scipy import signal
from scipy.interpolate import UnivariateSpline
from scipy.interpolate import interp1d

#Values for the Gaussian quadrature
```

The method we used to perform the integration was a Gaussian quadrature, the values for which are below.

```
x1=np.array([0.012223698960615764198052 1,0.036663790968733493330215 3,
0.061081969604139568103787 0,0.085463640504515498636498 0,
  0.109794231127643746672974 7,0.134059199461187785117575 3,
  0.158244042714224933997475 5,0.182334305985337182410382 6,
  0.206315590902079217154058 0,
```

```
    0.23017356422665998641098 66,0.25389396642269432085561 80,
    0.27746262017790440280623 16,0.30086543887767720266715 41,
    0.32408843502441337518325 23,
    0.34711772859763550842616 28,0.36993955534985902661659 17,
    0.39254027503326744273564 82,0.41490637955227501549227 39,
    0.43702450103710416293704 29,
    0.45888141983355219544908 91,0.48046407240417202585827 57,
    0.50175955913614446428960 63,0.52275515205117547845394 79,
    0.54343830241281036344419 36,
    0.56379664822661808391443 08,0.58381802162876308955003 89,
    0.60349045615854862420357 32,0.62280219391058491076153 96,
    0.64174169256230755715352 49,
    0.66029763227264605210594 68,0.67845892244771925936775 57,
    0.69621470836951433238508 66,0.71355437768358741334385 99,
    0.73046756674190880647173 69,
    0.74694416679706198116988 24,0.76297433004409472277976 91,
    0.77854847550641196685049 41,0.79365729476219329024333 29,
    0.80829175750791366011964 22,
    0.82244311695564384246459 42,0.83610291506090684711687 53,
    0.84926298757796896916360 01,0.86191546893954846059063 23,
    0.87405279695803179869541 80,
    0.88566771734539721740829 24,0.89675328804915818438644 74,
    0.90730288340175681392148 59,0.91731019808096053703648 36,
    0.92676925087894784333462 45,
    0.93567438827791637578312 68,0.94402028783022018212111 14,
    0.95180196134126438621779 63,0.95901475785369992809891 85,
    0.96565436643196526864582 90,
    0.97171681874713658090433 84,0.97719849146390738716537 44,
    0.98209610843571853602476 56,0.98640674272458620887123 55,
    0.99012781849173438333793 03,
    0.99325711290021293530343 72,0.99579275853498116686416 12,
    0.99773324862551401988215 74,0.99907745997737589501198 78,
    0.99982488794713191447360 81])

w=np.array([0.02444618019626251821132 59,0.02443156909785004505485 86,
0.02440235563384958209329 80,0.02435855726469062585326 85,
0.02430020016797186532344 26,0.02422731922281524812009 33,
0.02413995798901928499771 67,0.02403816868102405263758 73,
```

```
0.023922012136703455672450 4,
0.023791557781003400638780 7,0.023646883584447615143651 4,
0.023488076016535913153025 3,0.023315229994062760122415 7,
0.023128448824387027879297 9,
0.022927844143686846920411 0,0.022713535850236461309712 6,
0.022485652032744966871824 6,0.022244328893799765104629 1,
0.021989710668460491434122 1,
0.021721949538052075375261 0,0.021441205539208460137111 9,
0.021147646468221348537019 5,0.020841447780751149113583 9,
0.020522792486960069432285 0,
0.020191871042130041180673 2,0.019848881232830862219944 4,
0.019494028058706602823021 9,0.019127523609950945486518 5,
0.018749586940544708650919 5,
0.018360443937331343221289 3,0.017960327185008685940196 9,
0.017549475827117704648706 9,0.017128135423111376830681 0,
0.016696557801589204589091 5,
0.016255000909785187051657 5,0.015803728659399346858965 6,
0.015343010768865144085990 9,0.014873122602147314252385 5,
0.014394345004166846176823 9,
0.013906964132951985244288 0,0.013411271288616332314489 0,
0.012907562739267347220442 8,0.012396139543950922968821 7,
0.011877307372740279575891 1,
0.011351376324080416693281 7,0.010818660739503076247659 6,
0.010279479015832157133215 3,0.009734153415006805863548 3,
0.009183009871660874334478 7,
0.008626377798616749704978 8,0.008064589890486057972928 6,
0.007497981925634728687672 0,0.006926892566898813563426 7,
0.006351663161707187387214 3,
0.005772637542865698589334 6,0.005190161832676330205070 8,
0.004604584256702955118290 5,0.004016254983738642313194 3,
0.003425526040910215774337 8,
0.002832751471457991095285 7,0.002238288430962618743622 1,
0.001642503018669029538790 9,0.001045812679340348779312 9,
0.000449380960292090376394 3])


#Defining the 2 Gauss function
def twogauss(x, amp, cen, wid1, wid2):
```

```
    output=np.piecewise(x,[x<cen, x>=cen],
    [lambda x: amp*np.exp(-(x-cen)**2/wid1),
    lambda x: amp*np.exp(-(x-cen)**2/wid2)])
    return output

#testing the twogauss function
#xtest=np.linspace(-10,10)
#ytest=twogauss(xtest,5,3,.5,10)
#plt.plot(xtest,ytest)

sig1s=[]
sig2s=[]
datalist=[]
intsS=[]
intsL=[]
penline=0
```

This while loop reads each event in a data file, plots it, calculates the integrals for the long and short intervals, and stores those values.

```
line=f.readline()

while line:
    if line.startswith('EVENT', 4, 10):
        L1=line.rsplit()
        eventnostr=L1[2]
        eventno=int(L1[2])
        print('Event: %s' % eventnostr)
    if penline==1:
        datastr=line
        datasplit=line.rsplit()
        for i in datasplit:
            data=float(i)
            datalist.append(data)
        datalen=len(datalist)
        #print('datalen:',datalen)
        x=np.linspace(0,datalen,datalen)
        xt=2.5*x
```

```
mi=np.argmax(datalist)
m=np.amax(datalist)
#Now for the integration
#Pick a spline or interpolation. We might pick any of the curve
#fit functions but idk
#f2 = interp1d(xdata, ydata, kind='cubic')
spl=UnivariateSpline(xt,datalist)
#This is the short gate
aS=xt[mi]-300
bS=xt[mi]+500
integralS=0.
for i in range(63,-1,-1):
    integralS+= w[i]*spl((bS-aS)/2. *(-x1[i]) + (aS+bS)/2.)
    #integral+= w[i]*spl((b-a)/2. *(-x1[i])+(a+b)/2.)
    # integral = integral + ___
for i in range(0,63,1):
    integralS+= w[i]*spl((bS-aS)/2. *x1[i] + (aS+bS)/2.)
    #integral+= w[i]*spl((b-a)/2. *x1[i]+(a+b)/2.)
integralS *= (bS-aS)/2.
intsS.append(integralS)
#print('Short Integral:',integralS)
#the long gate
aL=xt[mi]-300
bL=xt[mi]+1500
integralL=0.
for i in range(63,-1,-1):
    integralL+= w[i]*spl((bL-aL)/2. *(-x1[i]) + (aL+bL)/2.)
    #integral+= w[i]*spl((b-a)/2. *(-x1[i])+(a+b)/2.)
    # integral = integral + ___
for i in range(0,63,1):
    integralL+= w[i]*spl((bL-aL)/2. *x1[i] + (aL+bL)/2.)
    #integral+= w[i]*spl((b-a)/2. *x1[i]+(a+b)/2.)
integralL *= (bL-aL)/2.
intsL.append(integralL)
plt.plot(xt,datalist)
plt.title('Event %s' % eventno)
plt.ylabel('Voltage')
plt.xlabel('Time (ns)')
```

```
            plt.vlines([aS,bS],0,m,colors='r')
            plt.vlines([aL,bL],0,m,colors='g')
            #print('Long Integral:',integralL)
            plt.savefig('IntWithMaxAllT2/Event %s.png' % eventno)
            plt.clf()
            del datalist[:]
            penline=0
        if line.startswith('CH:', 4, 7):
            L2=line.rsplit()
            channelnostr=L2[2]
            channelno=int(L2[2])
            #print('Channel: %s' % channelnostr)
            penline=1
        line=f.readline()
f.close()
```

The following code writes the calculated integral values to a file.

```
IntWithMaxAllTS2=open('IntWithMaxAllS2','w+')
intstr=str(intsS)
IntWithMaxAllTS2.write(intstr)

IntWithMaxAllTL2=open('IntWithMaxAllL2','w+')
intstr=str(intsL)
IntWithMaxAllTL2.write(intstr)
```

Here is the code I used to calculate the ratio of the long integral and the short integral, and then plot this ratio against the waveform's amplitude.

```
# -*- coding: utf-8 -*-
"""
Created on Tue Jun 14 11:48:45 2016

@author: grgroup
"""
import matplotlib.pyplot as plt
import matplotlib.mlab as mlab
import json
import numpy as np
from scipy.optimize import curve_fit
```

```
IntWithMaxS=open('IntWithMaxAllS2','r')
intsSMax=IntWithMaxS.readline()
ShortIntsMax=json.loads(intsSMax)
SIMax=np.array(ShortIntsMax)

IntWithMaxL=open('IntWithMaxAllL2','r')
intsLMax=IntWithMaxL.readline()
LongIntsMax=json.loads(intsLMax)
LIMax=np.array(LongIntsMax)

#IntWithMeanS=open('IntWithMeanS','r')
#intsSMean=IntWithMeanS.readline()
#ShortIntsMean=json.loads(intsSMean)
#SIMean=np.array(ShortIntsMean)

#IntWithMeanL=open('IntWithMeanL','r')
#intsLMean=IntWithMeanL.readline()
#LongIntsMean=json.loads(intsLMean)
#LIMean=np.array(LongIntsMean)

PSDMax=(LIMax-SIMax)/LIMax
#PSDMean=(LIMean-SIMean)/LIMean

TwoGAmps=open('TwoGAmps','r')
amplitudes=TwoGAmps.readline()
amps=json.loads(amplitudes)

plt.plot(amps,PSDMax,'bo')
#plt.plot(amps,PSDMean,'ro')
plt.title('PSD (found with max) vs Amplitude')
plt.xlabel('Amplitude')
plt.ylabel('PSD')
plt.savefig('PSDvAmpMax20160707a2')

#plt.clf()

#plt.plot(amps,PSDMean,'ro')
```

```
#plt.title('PSD (found with mean) vs Amplitude')
#plt.xlabel('Amplitude')
#plt.ylabel('PSD')
#plt.savefig('PSDvAmpMean20160707a')

#TwoGSig1s=open('TwoGSig1s','r')
#sigmas1=TwoGSig1s.readline()
#sig1=json.loads(sigmas1)

#TwoGSig2s=open('TwoGSig2s','r')
#sigmas2=TwoGSig2s.readline()
#sig2=json.loads(sigmas2)



IntWithMaxS.close()
IntWithMaxL.close()
#IntWithMeanS.close()
#IntWithMeanL.close()
TwoGAmps.close()
```

Appendix B

The second project: profiling a cesium iodide detector

Another project my partner and I worked on was to measure the energy resolution across the faces of two cesium iodide (CsI) detectors. This project was unrelated to MIνER, but the CsI detectors would later be used in other experiments.

About energy resolution

A detector's response function is the differential pulse height distribution a detector might produce when measuring radiation of a specific known energy. The closer this distribution is to a single spike or delta function, the better the detector's energy resolution is said to be. The resolution of a detector is formally defined as

$$R = \frac{FWHM}{H_0} \tag{B.1}$$

where FWHM is the full-width at half-maximum of the distribution and H_0 is the peak's height. The FWHM is defined as the peak's width when the frequency is half of the peak's maximum value. This definition assumes that any background noise has been subtracted out of the distribution or can be ignored. The smaller the energy resolution, the better the detector can distinguish between particles with similar energies.

The project

My research partner and I profiled two CsI detectors. A photograph of one of the detectors is in Fig. B.1. We measured the energy resolution across various points on each detector's face. We used a mixed alpha source (containing Gd-148, Pu-239, Am-241, and Cm-244), and each profiled a separate detector. ^{148}Gd has a peak energy

of 3177.75 keV, ^{239}Pu has a peak energy of 5142.60 keV, ^{241}Am has a peak energy of 5472.12 keV, and ^{244}Cm has a peak energy of 5787.68 keV. Fig. B.2 shows these energy peaks.

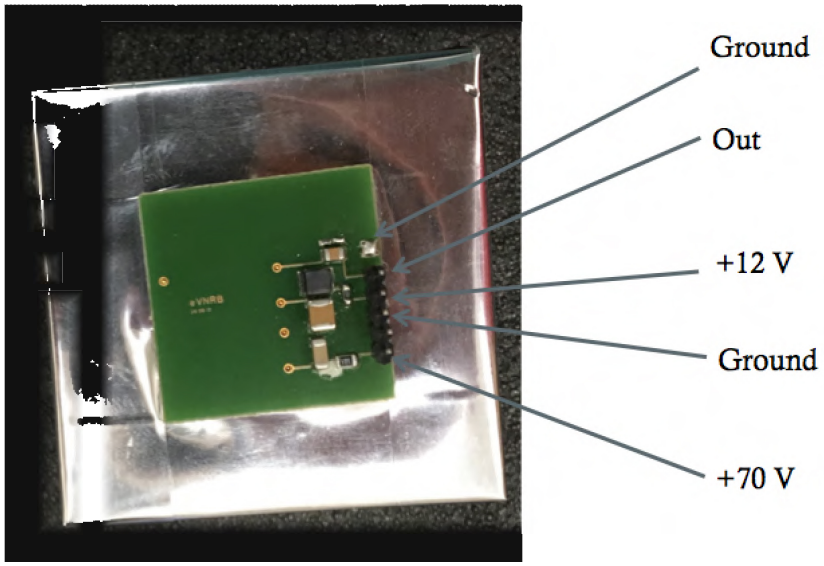

Figure B.1: A photograph of the detector with the pins labelled.

To test small areas of the detector's surface at a time, we created a plastic mask (shown in Fig. B.3) to place between the detector's surface and the mixed alpha source. It contains a grid of holes, with each hole being 3mm by 3 mm. The mask itself was 50 mm by 50 mm, to match the dimensions of the detector. To test one hole at a time, we would tape over all of the other holes. Alpha radiation is heavy enough that it is blocked by the tape. For the measurements, we placed the detector and the alpha source in a vacuum chamber. For each measurement, we tightly sealed the chamber, used a vacuum pump to slowly pump out the air, and then turned the pump off. This was done so that we would have a higher rate of alpha particles incident on the detector, as they only travel a few centimeters in air. We used pulse counting mode, which recorded the energy and number of alpha particles that passed through each hole. The experimental setup is shown in Fig. B.4. A diagram of the electronic setup is shown in Fig. B.5.

As we used a combined alpha source, we expected to see four energy peaks: one from each nuclide. We recorded the means and FWHMs of each peak. From these values, we calculated the means and sigmas for each hole.

^{148}Gd, the nuclide with the lowest energy peak, frequently didn't show up in the

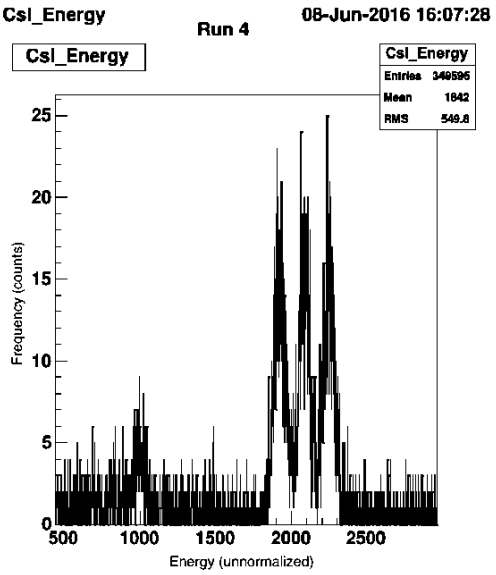

Figure B.2: This graph shows a measurement of the mixed alpha source. The x-axis shows the particles' energy (though it is uncalibrated) and the y-axis shows the counts.

measurements, so it was excluded from the results. Graphs showing the means and resolutions for the detector I tested are in Fig. B.6-B.8 and B.9-B.11. Each square on a graph represents a single hole in the mask. Each square's location on the graph matches up with each hole in the mask in the picture shown in Fig. B.3; the holes and squares are shown as if one is looking towards the detector's face.

The peak means measured by the detector do vary across various places on the detector's surface. The overall resolution of the detector was found to be about 4%. This non-uniformity across the detector's face contributed about 1% to the detector's overall resolution. This energy resolution is sufficient for the experiments in which these detectors will be used. These detectors will be part of an active-target time projection chamber, called TexAT, currently in development. These CsI detectors will be placed behind Si detectors to catch radiation that may have escaped or passed through the Si detectors.

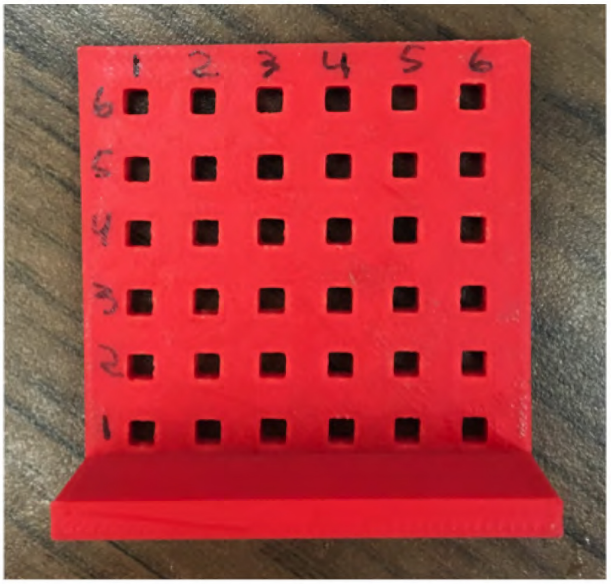

Figure B.3: A photo showing the mask used to test small areas of the detector's face at a time.

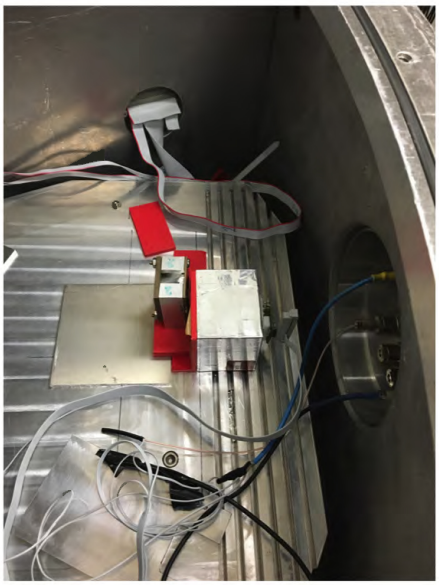

Figure B.4: A photo showing the setup of the CsI profiling measurements.

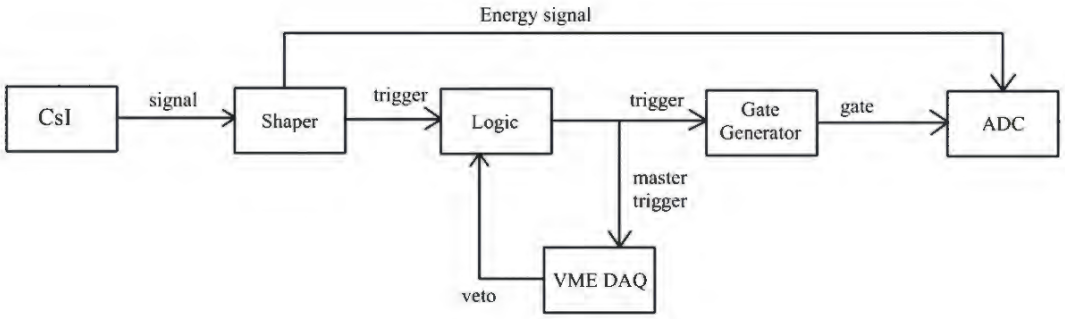

Figure B.5: A diagram showing the setup of the electronics.

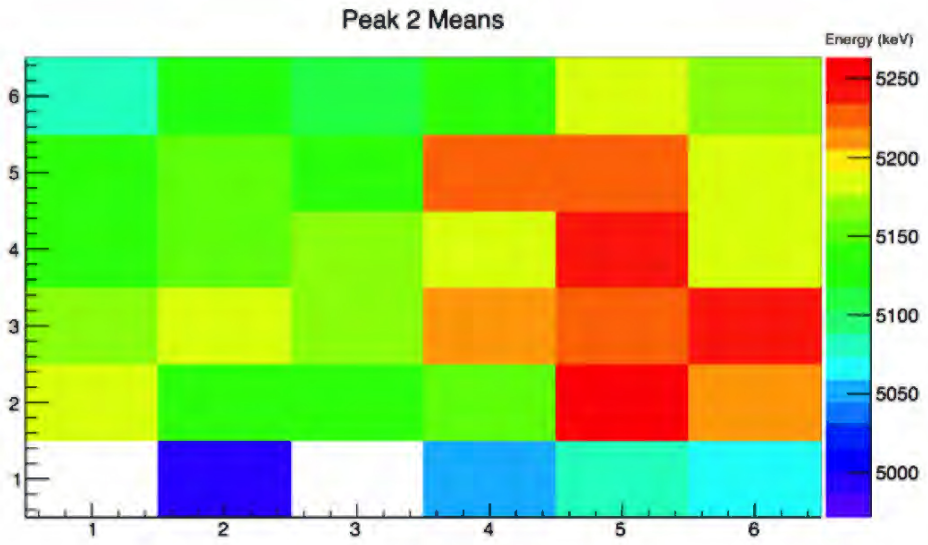

Figure B.6: A plot showing the mean of the ^{239}Pu peak for each hole. Each square corresponds to a hole in the mask. The graph is arranged as if one was looking towards the face of the detector.

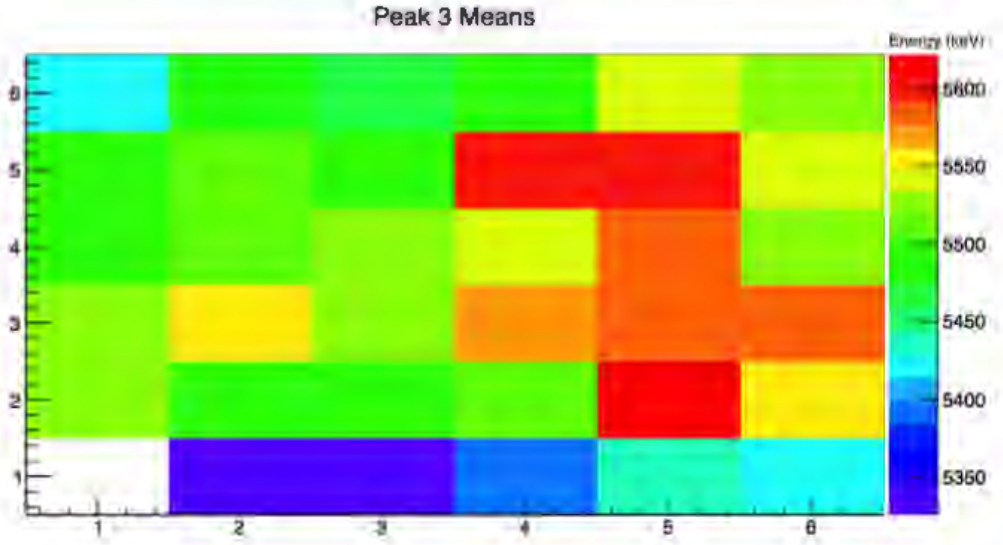

Figure B.7: A plot showing the mean of the ^{152}Eu peak for each hole. Each square corresponds to a hole in the mask. The graph is arranged as if one was looking towards the face of the detector.

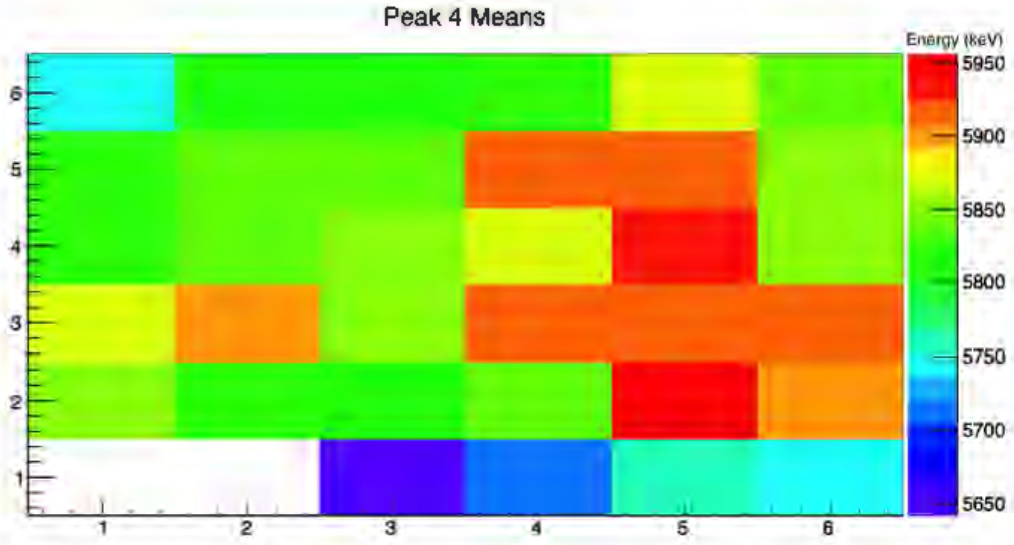

Figure B.8: A plot showing the mean of the ^{244}Cm peak for each hole. Each square corresponds to a hole in the mask. The graph is arranged as if one was looking towards the face of the detector.

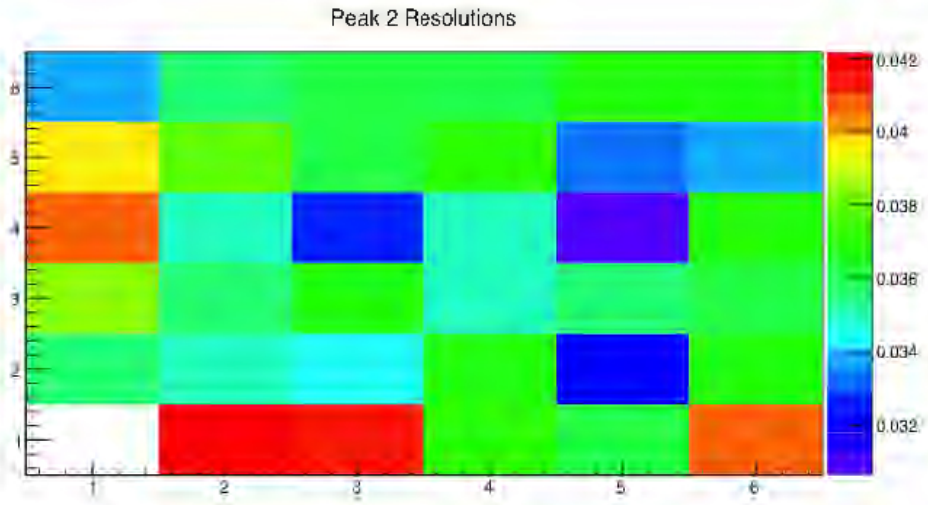

Figure B.9: A plot showing the resolution for the ^{239}Pu peak for each hole. Each square corresponds to a hole in the mask. The graph is arranged as if one was looking towards the face of the detector. The resolution only varies by about one percent across the detector's surface.

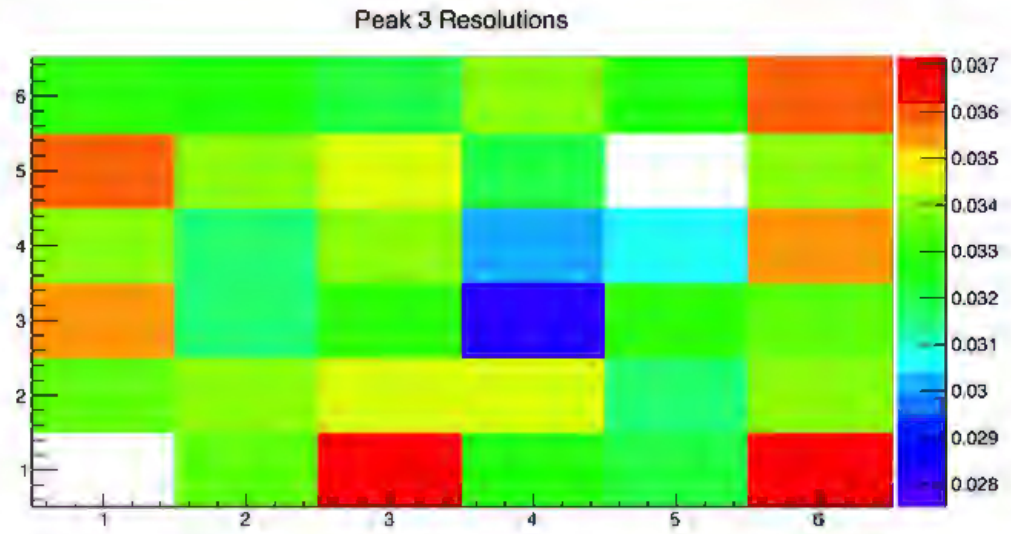

Figure B.10: A plot showing the resolution for the ^{152}Eu peak for each hole. Each square corresponds to a hole in the mask. The graph is arranged as if one was looking towards the face of the detector. The resolution only varies by about one percent across the detector's surface.

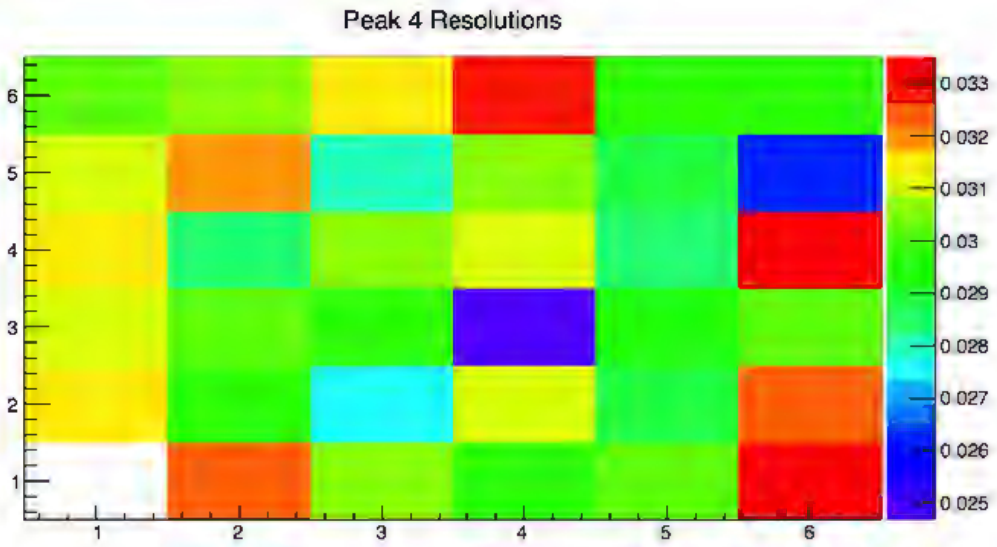

Figure B.11: A plot showing the resolution for the ^{244}Cm peak for each hole. Each square corresponds to a hole in the mask. The graph is arranged as if one was looking towards the face of the detector. The resolution only varies by about one percent across the detector's surface.